Mechanical Resonators Based on Graphene and Carbon Nanotubes

Thesis by
Ioannis Tsioutsios

June 2016

Doctoral school in Physics, Universitat Autònoma de Barcelona (UAB)
ICFO - The Institute of Photonic Sciences

Supervisor: Prof. Dr. Adrian Bachtold
Tutor: Prof. Dr. Jordi Pascual Gainza

Thesis committee:
Prof. Dr. Francisco Javier Tamayo de Miguel
Prof. Dr. Jean-Philippe Poizat
Prof. Dr. Romain Quidant

ICFO
Institut de Ciències Fotòniques

UAB
Universitat Autònoma de Barcelona

Chapter 7

Hybrid nano-optomechanics based on carbon nanotube resonators

In this chapter we will describe the first steps towards studying suspended doubly-clamped singly-walled carbon nanotubes, at low temperature, as hybrid nano-optomechanical systems. This work has been carried out in collaboration with Professor François Dubin (Institut des nanosciences de Paris (INSP), Pierre and Marie Curie University - Paris 6) and the group of Professor Frank Koppens (Nano-Optoelectronis group, The Institute of Photonic Science (ICFO)).

In the first section we give a brief introduction on the objectives of this project. We then discuss the role of excitons in the optical properties of single-walled carbon nanotubes and how their coupling to the mechanical vibrations of suspended nanotubes can form the bases a hybrid nano-optomechanical system. We then present the fabrication process steps and the layout of the doubly-clamped suspended carbon nanotube devices that were used in this experiment, while we also discuss the various technological challenges. Afterwards, we describe the low temperature optical setup that we developed for the purposes of this study. We then present the experimental data that we obtained, analyzing them and discussing the technical challenges that we faced. Finally, we discuss the perspectives of such an experiment taking into account the knowledge that was acquired so far.

7.1 Introduction

In recent years, there has been a great amount of experimental effort in order to prepare, observe and control the motion of a mechanical resonator in the quantum regime. Such experiments require the ability to cool a mechanical mode into its ground state ($T \ll hf/k_B$), to create and control individual quantums of excitation (phonons), and detect them with quantum-limited sensitivity (Heisenberg limit). In this direction, different approaches have been followed.

The emerging field of cavity opto- and electromechanics has tried to achieve the aforementioned goals by coupling a mechanical resonator to a microwave or an optical cavity. In such systems, the phase of the cavity light field linearly depends on the position of the mechanical oscillator. At the same time, the light field applies a back-action force on the resonator due to radiation pressure. In experiments with such systems, it has been

demonstrated that it is possible to actively cool the motion of a mechanical resonator to its ground state while detecting its mechanical vacuum fluctuations [8, 9]. Additionally, evidence of back-action quantum noise has also been observed [10]. However, lineal position measurements impose limitation when used to manipulate quantum states on the mechanical resonator. This occurs because the noise of the cavity field can be disguised as mechanical fluctuations, blurring non-classical states of motion.

An alternative approach is to couple a mechanical resonator to a quantum system, like a two-level system, that can be externally controlled. O'Connell *et al.* (2010) [7] in their pioneer experiments they used an engineered hybrid device, where a superconducting phase qubit is capacitively coupled to a micromechanical resonator, in order to perform quantum-coherent measurements and for the first time provide strong evidence that quantum mechanics applies to motion of objects that are big enough to be seen by naked eye [7]. The qubit can be approximated as a two-level quantum system, while a cryogenic refrigerator was used to cool a 6 GHz mode of the mechanical resonator to its ground state.

Advances in nanotechnology have lead to a new type of hybrid nanomechanical systems where quantum emitters are embedded into the bulk of mechanical nanoresonators. Such type of devices have the potential to achieve a large coupling strength through the deformation potential [161]. Yeo *et al.* (2013) [162] studied a hybrid system that consist of a GaAs conical photonic nanowire with optically active InAs quantum dots [162] that are embedded in it. He demonstrated that the strain mediated coupling between the energy levels of the quantum dots and the mechanical degrees of freedom of the nanowire lead to an ultra strong exciton-phonon coupling. Experiments in a similar direction have shown that it is possible couple the motion of a diamond mechanical resonator to Nitrogen-Vacancy (NV) center spins, [163], or the motion of MBE-grown GaAs/AlGaAs coreâĹŠshell nanowires to optically active quantum dots that are build into it [164].

Within the context of hybrid nanomechanics, single-walled carbon nanotube resonators qualify as very attractive systems to explore. From the perspective of nanomechanics, their exceptional mechanical properties have lead to devices with very high resonant frequencies [14, 15], high quality factors [17], and remarkable mass and force sensitivity [20, 23]. For experiments in the quantum regime, high frequencies allow for low phonon number occupation in cryogenic temperatures, their low mass ensures large zero point motion ($x_{\mathrm{zpm}} = \sqrt{\hbar/2m\omega_{\mathrm{m}}}$), about three orders of magnitude higher compared to top-down fabricated resonators, and their high quality factors secures long coherence times. Interestingly, these nano-scale objects are also inherited with very rich electronic and optical properties. It has been shown that optical transitions in single-walles semiconducting nanotubes are dominated by excitons [165], which are electron-hole bound states. In addition, it has been demonstrated that individual suspended carbon nanotubes can host localized excitons that exhibit very high luminescence quantum efficiency as well as very long decay and coherence times [166, 167]. A localized exciton can be seen as an optically active quantum dot, a two-level system, that is intrinsically embedded inside carbon nanotubes.

Theoretical studies have shown that excitonic resonances of carbon nanotubes could exhibit strong parametrical coupling to flexural motion via strain, which modifies the deformation potential electron-phonon interactions [168, 169]. The existence of such a coupling mechanism could lead to a novel hybrid nanomechanical system, where a single walled-carbon nanotube resonator is coupled to a quantum emitter embedded into it. This

type of interaction could potentially used to cool a mechanical oscillator to its ground state [170] and study nanomechanics in the quantum regime by achieving quantum-limited position sensitivity and creating non-classical states of motion [7]. In a more short-term perspective, an optical transduction scheme based on exciton-phonon coupling, could possible improve the displacement sensitivity limits of electrical or optical transduction schemes used so far in carbon nanotubes resonators [86, 23].

In this chapter, we present the first steps towards the experimental investigation of suspended single-walled carbon nanotubes as hybrid nanomechanical systems. In this direction, we developed and systematically studied the fabrication process of suspended singly-walled carbon nanotubes, while we developed and implemented a low-temperature micro-photoluminescence optical setup. The main target was to study the existence of exciton-phonon coupling and the underlying physical mechanisms in such devices. Even though it wasn't possible to reach the final goals within the time frame of this Ph.D thesis, we nevertheless tried to systematically describe and analyze all the drawbacks and difficulties we faced, trying to give a perspective for the future steps towards the completion of such an experiment.

7.2 The role of excitons in the optical properties of single-walled carbon nanotubes

In section 2.3 we described the optical transition of single-wall carbon nanotube as band to band transitions (Figure 2.7), where an electron-hole pair is optically excited from the valence band into the conduction band, emitting a photon while recombining. Light absorption at photon energy E_{22} is followed by fluorescence emission near E_{11} (Figure 7.1(a)), where E_{11} and E_{22} are characteristic values for each nanotube specie (n_1, n_2) and correspond to the transitions energies between the van-Hove singularities that appear in electronic states density of nanotubes. Attributed to the linear conic dispersion and electron-hole symmetry around the K point of the graphene band structure, the expected ratio between the second and first optical transitions is $E_{22}/E_{11} = 2$. Interestingly, experimental studies have shown that this ratio is closer to ~ 1.7 [171] (Figure 7.1(b)).

The reason of divergence between experiment and theory is that so far we have followed a single particle description, neglecting many-body interactions. In reality, the low screening of electrostatic interactions and the strong confinement of carriers in one dimension leads to Coulomb interactions that are considerable enhanced in carbon nanotubes. On the one hand, the electron-electron repulsion tends to blue-shift the energies and renormalize the effective band-gap, an effect which is difficult to be quantified experimentally. On the other hand, the electron-hole attraction leads to bound electron-hole states instead of free electron-hole pairs. A state like this is called exciton and can be seen as a quasiparticle with neutral charge. Their energy is much lower compare to what is expected in optical transition due to the van-Hove singularities in the density of states of the single-particle picture [165, 171]. The difference in energy is called the binding energy and it can be significant for single-walled nanotubes with low diameters [172]. Theoretical estimations predict that it exceed few hundreds of milli-electronvolts for tubes with diameter that is lower than 1 mm, and scales inversely with the diameter ($\sim 1/d$) [173, 174].

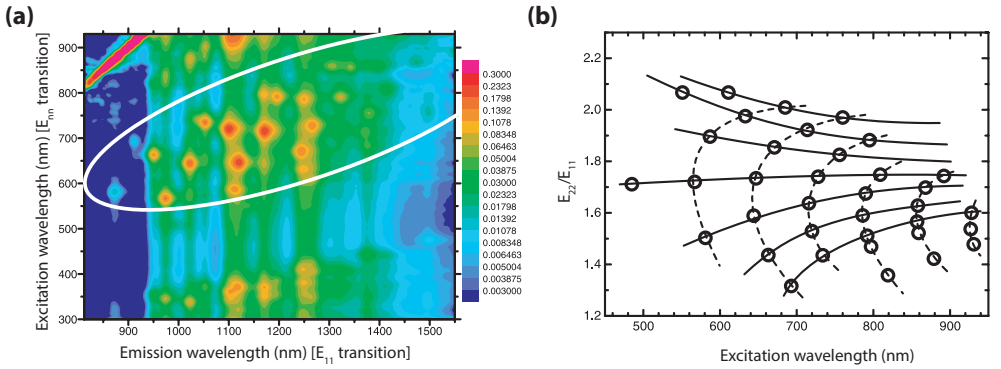

Figure 7.1: Photoluminescence measurements and transition energies characterization for large number of single-walled carbon nanotubes done by Bachilo *et al.* in 2002. **(a)** A typical contour plot of fluorescence intensity versus excitation and emission wavelengths for a sample of SWNTs. The E_{11} emission is enhanced when the excitation energy muches the E_{22} transition. **(b)** Measured ratios of excitation to emission frequencies for peaks shown in, plotted versus excitation wavelength. Solid and dashed lines show perceived patterns. Figure adapted from [171].

In 2005, Wang *et al.* experimentally confirmed for the first time that the optical properties of single-walled carbon nanotubes are dominated by excitons [165]. In this experiment, the exciton states where treated analogously to the hydrogenic states (Figure 7.2). By using a two-photon excitation spectroscopy binding-energies of ~ 400 meV were found for single-walled carbon nanotubes with 0.8 nm diameter. This value is about an order of magnitude larger than that for exciton in II-VI or III-V semiconductor quantum dots.

Despite the attractive intrinsic optical properties of semiconducting single-walled carbon nanotubes, their quantum-yield [1] and radiative lifetimes have been rather low [175]. This behavior is attributed to various intrinsic or extrinsic mechanisms. On the one hand, extrinsic non-radiative recombination happens when highly-mobile excitons explore defects and dopands along the nanotube [167]. On the other hand, intrinsic dark-exciton states affect the photoluminescence (PL) efficiency at temperature below 50 K [176]. However, in recent experiments it has been demonstrated that it is possible to get semiconducting single-walled carbon nanotubes with very high photoluminescence quantum-yield, radiative life times close to the intrinsic theoretical predictions as well as long dephasing times [166, 177]. Hofmann *et al.* (2013) [166] succeed to get very bright excitons, in suspended as-grown single-walled carbon tubes, with radiative lifetime of 3.35 ns and resolution limited spectral linewidth of $\sim 40\ \mu eV (\sim 10\ GHz)$ (Figure 7.3). Similar high values, have also be demonstrated by Sarpkaya *et al.* (2013) [177] in ultra clean suspended nanotubes. This high performance arise from the localization of exciton states in the tube, which emerges naturally in as grown suspended nanotubes. Essentially these zero-dimensional like excitons behave like optically active quantum dots where localization protects them from exploring photoluminescence quenching sites. Additionally, it has been demonstrated that it is also possible to localize excitons and increase their brightness by chemically modifying them [167].

[1] Quantum-yield of an optical emitter is the emitted photons per absorbed photon.

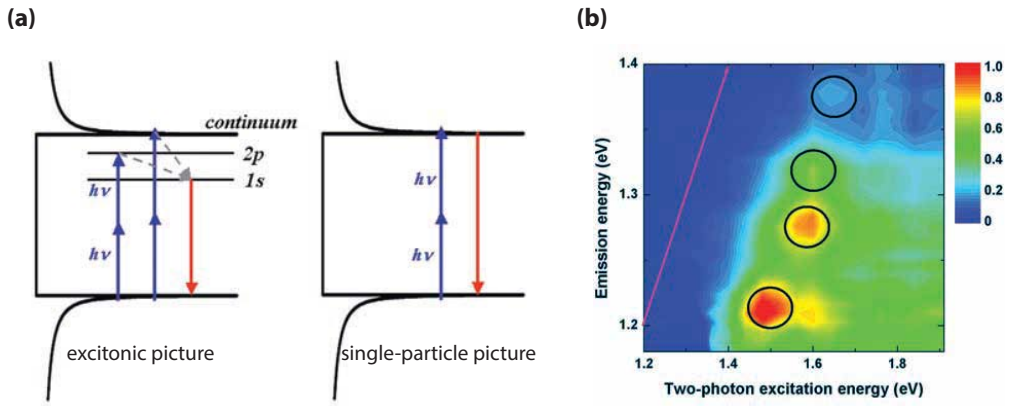

Figure 7.2: Two-photon excitation experiment done by Wang *et al.* (2005) [165]. **(a)** A schematic representation of the density of states in single-walled carbon nanotubs. Left side: In the exciton picture, the 2p and 1s states lie below the continuum of states in the band-gap. The 1s exciton state is forbidden under two-photon excitation. The 2p exciton and continuum states are excited. They relax to the 1s exciton state and fluoresce through a one-photon process. Right side: In the single-particle picture, the threshold for two-photon excitation lies at the band edge. The relaxation fluorescence emission energy is defined by the van-Hove singularities. **(b)** Contour plot of two-photon extcitation spectra of single-walled carbon nanotubes. The two-photon excitation energy is shown in the x-axis and the single-photon emission energy in the y-axis. The two-photon excitation peaks are shifted substantially above the energy of the corresponding emission feature, as is apparent by comparison with the single-particle picture where excitation and emission energies are equal. The large shift arises from the excitonic nature of single-walled carbon nanotube optical transitions.

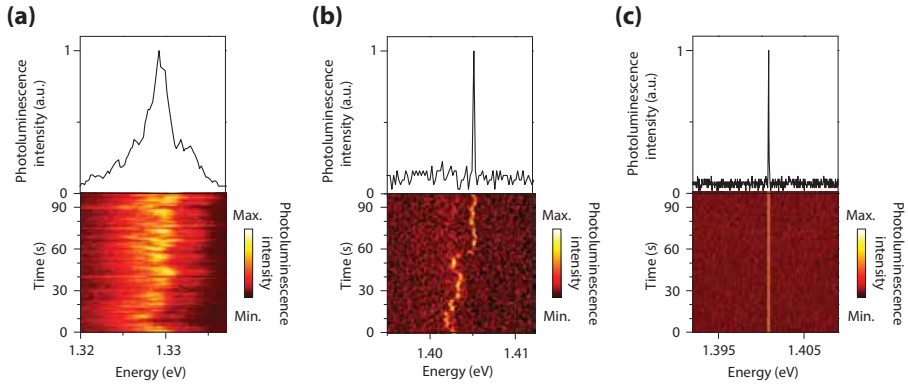

Figure 7.3: Role of spectral fluctuations in the photoluminescence lineshape in the experiment done by Hofmann *et al.* (2013) [166]. **(a-c)** Photoluminescence spectra measured in 1 s for a commercial micelle encapsulated CoMoCAT-nanotube on SiO_2 (a), a single as-grown nanotube on SiO_2 (b), and a single as-grown nanotube suspended over a SiO_2 crater (c).

7.3 Suspended single-walled carbon nanotubes as hybrid nano-optomechanical resonators

In a theoretical study in 2004, I.Wilson-Rae *et al.* [161] proposed a scheme where it is possible to cool a mechanical nanoresonator's mode to its ground state. The proposed system consist of a GaAs semiconducting beam structure with embedded InAs quantum dots (Figure 7.4(a)). As the beam vibrates, flexion induces extensions and compressions in the structure. As a result, the longitudinal strain will modify the energy of the quantum dot electronic states through deformation potential coupling [178]. This strain mediated coupling between the mechanical degrees of freedom and the energy levels of the embedded two-level system leads to a new type of mesoscopic hybrid optomechanical systems, where coherent optomechanical transduction and sideband cooling schemes can be applied in a similar manner as in cavity optomechanical systems [9] and trapped ions [179, 180].

An experimental demonstration of such a system by Montinaro *et al.* (2014) [164] is shown in Figure 7.4(b,c). The mechanical vibrations of a GaAs/AlGaAs core - shell nanowire cantilever are upconverted to optical frequencies though strain mediated modification of the transition energy levels of a quantum dot that is embedded inside the structure. The mechanical vibrations will then appear as a blurring on the emission spectra of the quantum dot. The optically active quantum dot can be described as a two-level system with a ground state $|g\rangle$ and an excited state $|e\rangle$. Such a hybrid system is well described by the independent spin-boson Hamiltonian [181]

$$H = \hbar\Omega_0(a^\dagger a + 1/2) + \hbar\omega_0\sigma_z/2 + \hbar g_0\sigma_z(a^\dagger a + a), \tag{7.1}$$

where Ω_0 is the mechanical resonator eigenmode frequency, $\hbar\omega_0$ the quantum dot transition energy for the wire at rest, a the phonon annihilation operator, and $\sigma_z = |e\rangle\langle e| - |g\rangle\langle g|$ the Pauli operator of the two-level system. The interaction between the mechanical degrees of freedom and the two-level system is given by the vacuum coupling rate

$$g_0 = \frac{\partial\omega_0}{\partial x}|_{x=0}\ \delta x_{\mathrm{zpf}}, \tag{7.2}$$

where x is the amplitude of the mechanical eigenmode, $x = 0$ the equilibrium position, $\hbar\omega_0$ the quantum dot transition energy which depends on x, and δx_{zpf} the zero point fluctuation (zpf). Practically, g_0 describes how strong is the interaction between the quantum dot transition energy and the lattice deformation. When this value is comparable or exceeds the decoherence rate of the quantum dot T_2^{-1} as well as the mechanical damping rate γ_m various applications are accessible. A regime where g_0/Ω_0 is close to unity has been achieved in the system of Montinaro *et al.* (2014) [164] as well as in a similar hybrid optomechanical system from Yeo *et al.* (2013) [162]. However, non of these systems where close to a regime where g_0 exceeds the coherence time of the quantum-dots.

Similarly to the already reported hybrid optomechanical systems [162, 164], a suspended single-walled carbon nanotube, can be seen as a hybrid optomechanical system with nanoscale dimensions (Figure 7.5), where the localized zero-dimensional excitons behave like optically active quantum dots. The coupling rate g_0 of a such a system is likely to be rather strong [168, 169] leading to an exploration of new optomechanical regimes [170]. In Figure 7.5 a conceptual schematic of a carbon nanotube based hybrid optomechanical system is illustrated. As the carbon nanotube is vibrating, the transition energy

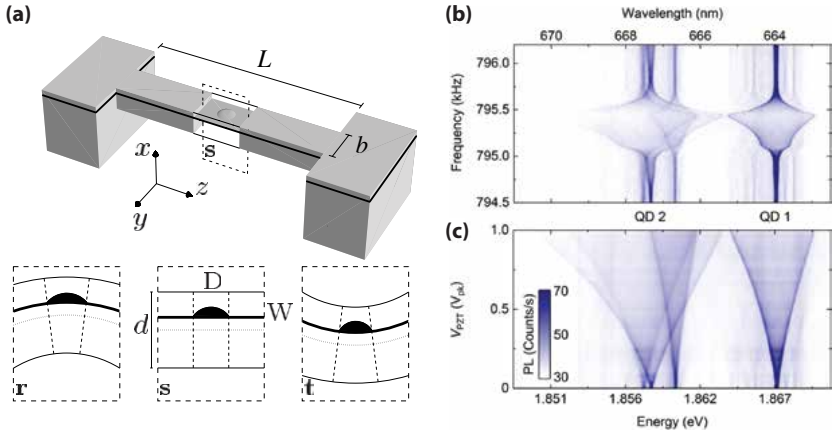

Figure 7.4: Optomechanical systems based on strain mediated coupling. **(a)** Top: Schematic diagram of a GaAs bridge, with an embedded InAs quantum dot. Bottom: Vertical cross sections through the axis of the bridge illustrating the deformations suffered by the quantum dot, when the beam is bent slightly in the vertical direction (x), modifying the energy level of the quantum dot. Figure adapted form [161]. **(b,c)** Emission spectra of a quantum dot that is embedded in a suspended single-clamped nanowire versus the mechanical actuation frequency and driving amplitude of the nanowire. When the nanowire is actuated on its resonant frequency, the emission energy of the the quantum dot is periodically modulated on the vibrational frequency, appearing as a blurring on the spectrometer. Figures (b) and (c) adapted from [164].

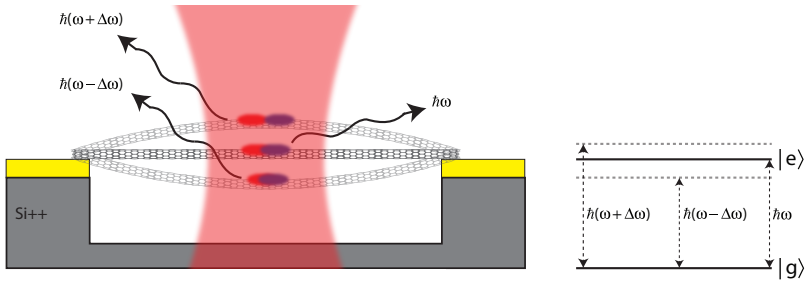

Figure 7.5: Conceptual schematic of an hybrid nano-optomechanical system based on singly-walled carbon nanotubes. A laser beam is used to excite the energy transition of a localized exciton. As the nanotube vibrates, the emission energy of the electrons is changing due to the modification of the deformation potential.

level of the localized excitons state will change through the modification of the deformation potential. The existence and the physical mechanisms of such an optomechanical coupling is the subject of the research effort that is described in this chapter.

7.4 Device layout and fabrication

7.4.1 Considerations and challenges

In order to meet the demands of this experiment, several consideration were taken into account regarding the layout and fabrication of the devices. Below the most important are listed:

Ultra clean carbon nanotubes

It is well known that the surrounding environment strongly affects the optical properties of carbon nanotubes. In particular, unintentional doping on their surface can cause no-radiative Auger process [182, 183] which can lead to blinking and spectral wondering of excitons [184]. The presence of such effects can reduce the performance of the system that we intend to study. Thus, for the purposes of this experiment, it is crucial to work with clean pristine optically active carbon nanotubes. For this reason, we developed a fabrication process where carbon nanotubes are grown at the very last step (subsection 7.4.2) avoiding the exposure to PMMA, evaporated metals, process chemicals and other materials that could possible contaminate and degrade their optical properties.

Low diameter nanotubes

The optical detection efficiency is one of the most important aspects of such an experiment. Most sensitive detectors (CCD camera or single photon counter avalanche photodetector) are found in the visible to near infrared (NIR). As we have seen earlier, due to high carriers confinement, carbon nanotubes with low diameter exhibit higher exciton and binding energies. In order to get nanotubes with photoluminescence emission in the visible to NIR, diameters below 1 nm are needed. Systematic control of this fabrication aspect is a non-trivial issue.

Individual suspended nanotubes

Photoluminescence quantum yield of semiconducting single-walled carbon nanotubes can be greatly decreased due to bundling (Figure 7.6). Excitons can decay non radiatively because of neighboring metallic nanotubes, leading to quenching of their photoluminescence efficiency [185]. We tried to tackle this issue by deterministically depositing and controlling the density of the used catalyst, as well as by working on the layout of the devices.

Sample layout

There are various parameters taken into account for the design and layout of the devices. An important one is the actuation mechanism for the flexural mechanical modes of the nanotubes. One way is to capacitively drive them using the N doped silicon substrate as a

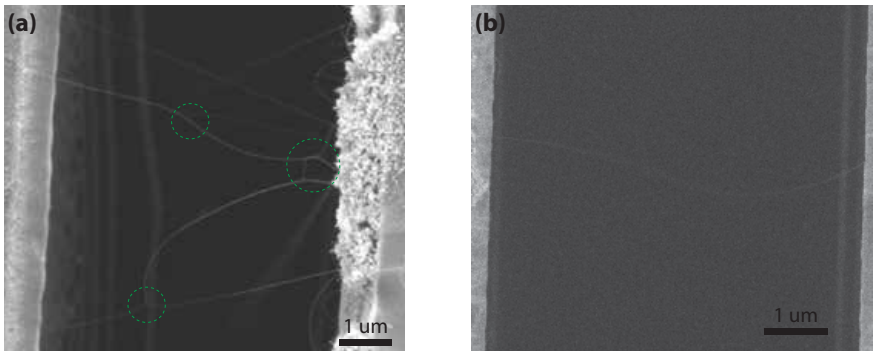

Figure 7.6: Bundling effect in carbon nanotubes. **(a)**. The excessive amount of catalyst near the trenches, leads to suspend nanotubes that form bundles. **(b)** An suspended individual carbon nanotube.

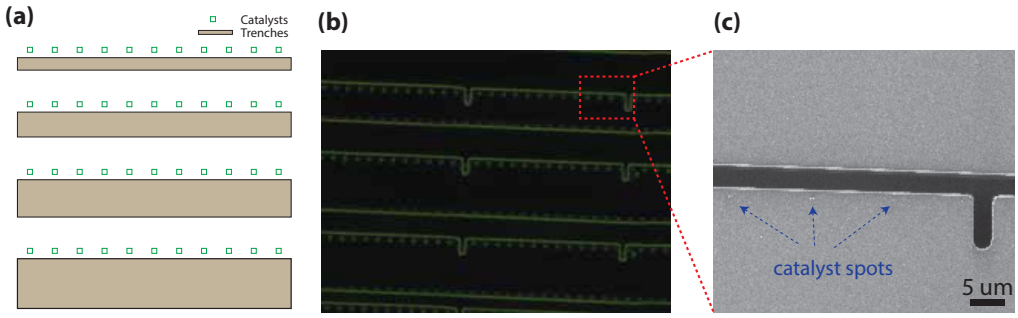

Figure 7.7: Sample layout. **(a)**. Schematic of the samples layout: green rectangle mask defines the openings for the catalyst and the brown mask defines the trenches. **(b)** An optical microscope image of a sample after the electron beam lithography step for the catalyst openings. The array of opening can been seen next to the trenches. **(c)** A scanning electron microscope image of a sample after the lift-off process. Catalyst spots can be identified.

back gate. The drawback of this approach is that the gate-field induced doping opens non radiative recombination channels and quenches the photoluminescence yield of nanotubes [186, 187]. The approach that we decided to follow is to mount the samples on top of a piezoelelctric actuator, and drive the nanotubes by inertial forces. The drawback here is that commercial piezoelectic actuators have cut-off frequency of few tenths of megahertz. Therefore we selected the length of the suspended part of the nanotubes to be in the range of 5 μm to 20 μm, leading to resonant frequencies in the kHz - MHz regime. Another key parameter is the depth of the trenches. We used a reactive ion etching process to achieve a depth of 10 μm, in order to avoid parasitic luminescence that does not originate from the nanotubes.

7.4.2 Fabrication process flow

The fabrication process starts by spin coating PMMA resist onto Si/SiO_2 substrate (Figure 7.8(a)). After an electron beam lithography (Figure 7.8(b)) and a reactive ion etching

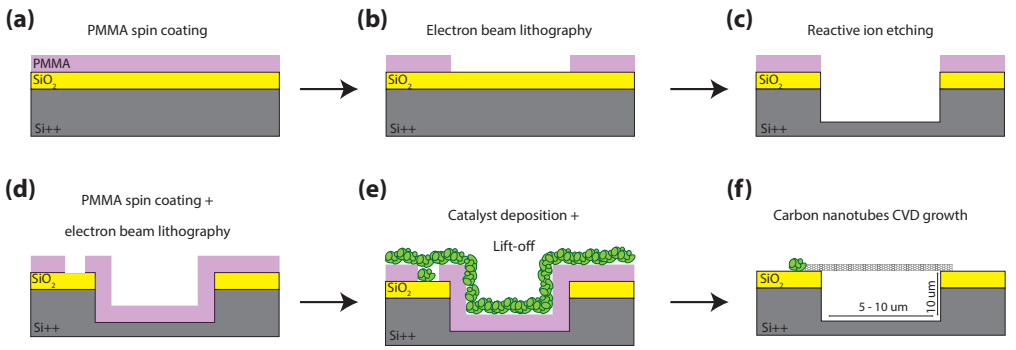

Figure 7.8: Fabrication process flow. **(a)** PMMA spin coating. **(b)** Electron beam lithography (EBL) used to define trenches. **(c)** Reactive ion etching is used to open the trenches. **(d)** Another PMMA spin coating and EBL step is used to create the opening for the catalyst deposition. **(e)** Catalyst deposition followed by a lift off process step. **(f)** Chemical vapor deposition (CVD) growth of carbon nanotubes.

step (Figure 7.8(c)), 10 μm deep trenches are opened. Another PMMA spin coating and electron beam lithography step are used to prepare openings before the catalyst deposition (Figure 7.8(d)). The catalyst solution is composed of Fe catalytic particle and Al_2O_3 while methanol is used as solvent. The deposition is done by covering the sample with few droplets of catalyst and leaving it to dry for 1-2 minutes. Then, by blowing the sample with a low nitrogen flow, only a thin layer of the catalyst covers the openings and the PMMA surface (Figure 7.8(e)). The samples are then baked for 5 min at 150 ^{o}C. For the lift-off process, the samples are left for 30 minutes in warm aceton and then are sonicated for 5 s to 10 s, depending on the sonication power. After the lift-off, islands of catalyst are found at the openings position. The growth of carbon nanotubes is done by chemical vapor deposition (CVD). In this step, thermal decomposition of a CH_4 vapor is achieved in the presence of a Fe catalyst. Nanotubes are growing from the catalyst island towards all directions. A fraction of them will be found suspended on top of the trenches (Figure 7.8(f)). The growth temperature can vary from 830 °C to 900 °C and the time from 2 to 10 min.

7.5 Confocal microscope setup

For the purposes of this experiment we built and developed a low temperature optical setup that is based around a confocal microscope and a 2.8 K base-temperature cryostat, with optical and electrical accesses [2]. Due to the wide range of single-walled carbon nanotubes with various chiralities and optical transition energies, the setup had to be achromatic in the widest possible wavelength range. We selected the components in order to be able to address the lowest diameter single-walled carbon nanotube species ((6,2),(6,4),(6,5),(7,0),(8,3),(9,1)), which have the highest binding energy. To overcome

[2]This setup has been designed so as to meet the long term goals of this project as well as for investigating mechanical resonators based on other materials such as graphene or other two-dimensional structures.

the low photoluminescence efficiency of nanotubes, the efficiency of the setup had to be maximized. The low temperature environment of the cryostat guaranties the lowest possible decoherence rate both for the mechanical modes of the suspended nanotubes and for the exciton states. The main parts of the setup are described below following the path of the light field from excitation to collection and detection (Figure 7.9):

- The excitation source is a continues wave (CW), narrow linewith, and widely tunable Titanium Sapphire laser (SolsTiS from M squared lasers Ltd). The excitation wavelengths range from 725 nm to 975 nm and the spectral linewidth is below 50 KHz. A 50:50 beam splitter is used in order to send a part of the output beam to a wavemeter that is used as an absolute frequency reference (HighFinesse WS-6 wavelength meter), while the other part is focused and coupled to a single mode optical fiber and then sent to the excitation path.

- On the excitation path, a lens is used to collimate light that is coming out of the fiber, followed by a high quality sharp short-pass filter. This filter is required in order to remove the broad background of light at longer wavelengths that is generated due to the strong inelastic scattering of the high intensity laser field inside the optical fiber. Since this background is at longer wavelengths than the excitation, it would otherwise be collected to the spectrometer, covering the signal expected from the optical resonances of the nanotubes.

- A half-waveplate and a polarized beam splitter are used to control the power and give an initial polarization to the laser beam.

- Another half-waveplate and a quarter-waveplate are used to fully control the polarization of the light field. The half-waveplate is used to polarize the beam along the tube axis in order to maximize the excitation efficiency. The quarter-waveplate is used to circularly polarize light, so as to maximize excitation efficiency when scanning large areas in order to find nanotubes that have random orientations on the chips.

- BS 1 is the central beam splitter of the setup. This component essentially defines the excitation and collection paths. Since there is plenty of availably excitation power from the Ti:S laser, this splitter is selected to be 10:90 (Reflection : Transmission) in order to maximize the efficiency of the collection path.

- The second beam splitter (BS 2) defines a secondary collection path that is used to acquire the reflection signal from the surface of the sample. This allows to image the surface of the devices and to optimize the focus.

- The following two beam splitters (10:90) combined with a LED source and a CMOS camera are used for real space imaging. This greatly facilitates the aligning of the setup, the focusing and finding the orientation on the sample. Both beam splitters are mounted on a flipping stage so as to be possible to be removed when performing photoluminescence experiments.

- An objective is used to focus the light field onto the samples, while it is placed outside the cryostat chamber, due to the limited available space inside. For this reason a high working distance objective was selected: a *100X Mitutoyo Plan Apo*

NIR HR infinity corrected objective which has 10 mm working distance and 0.7 numerical aperture (NA). It is mounted on top of a XYZ piezoelectric stage (Jena NV40 3 CLE) with a range of 100 μm $\times$ 100 μm and resolution of 2 nm. This allows to scan the surface of the devices with very high accuracy. The piezo and the objective are mounted on top of a millimeter accuracy XYZ position for coarse positioning.

- The samples our mounted inside a low vibration closed Helium cycle optical cryostat from Montana Instruments. The system has two principle stages, each with thermometers to accurately measure and control the temperature. The samples are mounted on the main stage which can reach base temperature of 2.8 K, while it can be also set in any value between 2.8 K and 300 K. A radiation shield is attached at the second stage, which is at 30 K. Hard vacuum is achieved using cryopumping charcoal absorbers. A critical feature of this system is the high level of vibrations isolation which is accomplished through active and passive damping techniques. Two glass windows (UQG spectrosil) are separating the sample from the objective. Both are selected to have the lowest possible thickness, 0.5 mm for the outer and 0.1 mm for the inner, in order to improve the light field collection efficiency. Furthermore, the system supports up to 4 RF and 4 DC lines in order to access electrically the studied devices. In the basic configuration, only one RF line is connected to a fast piezoelectric stage that is used to actuate the suspended nanotubes through inertia forces.

- Reflected, scatted and emitted light fields follow the same opposite path towards the primary collection path, apart from a fraction that is collected from the real space imaging path and from the secondary collection path. The first element of the primary collection path is a high quality sharp long-pass filter, which is needed to remove the reflected laser light which is orders of magnitude more intense than the PL signal and would otherwise saturate the spectrometer. The respective cut-off wavelengths of the short- and long-pass filters have to be carefully chosen. Their transmission ranges should not overlap, and their particular values also determine which nanotube chiralities can be detected and at what energies can be excited. At typical set of filter that we used have a cut-off at 830 nm, and this covers most of the chiralities that we are interested in and are detectable by our spectrometer (see spectrometer part). After filtering, the light field is focused in a single-mode optical fiber that its transmission efficiency is optimized for the emission wavelengths that we are interested in. This single-mode optical fiber plays the role of clear-aperture pinhole that is used in a conventional confocal microscope, but provides greater flexibility, less dust accumulation problems and easier alignment. The output of the fiber can be sent to a spectrometer, to an avalanche photodiode (APD) or any other desired detection and analysis equipment.

- The spectrometer is a 500 mm focal-length ANDOR Shamrock 500i. There are two grating installed: one with 600 l/mm ($\sim$ 150 μeV at 900 nm), which can reach a resolution close to 0.2 nm ($\sim$ 300 μeV at 900 nm), and another with 1200 l/mm which can reach a resolution close to 0.1 nm. The detector is a CCD camera from ANDOR (iDus 416), with 2000 $\times$ 256 pixel and maximum efficiency in near infrared (NiR).

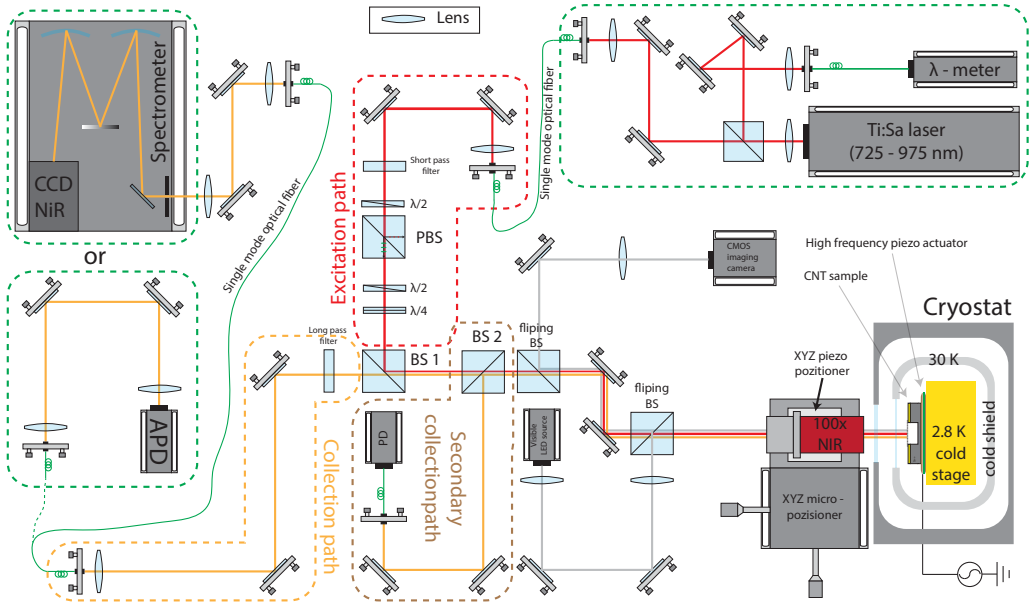

Figure 7.9: Semi-realistic schematic of the optical setup that was developed for the experiment. Details are given in the main text.

- Apart from the spectrometer, and single photon count avalanche photodiode (Excelitas SPCM-AQRH-15) is also installed on the setup.
- The interfacing of the setup has been done in Python using QTLab, an IPython-based measurement environment.

7.6 Experimental data

7.6.1 Characterization using phonon assisted excitation

In every fabricated sample a large variety of nanotubes with different chiralities and optical properties exist. It is therefore very challenging and time consuming to identify the tubes that are suspended, optically active, with low diameter, and detectable with our optical setup ((6,2),(6,4),(6,5),(7,0),(8,3),(9,1)). To achieve this, we run high resolution photoluminescence maps of 100 μm $\times$ 100 μm size (the range of the piezoelectric stage), at base temperature (2.8 K), using the piezoelectric stage. In principle, the most efficient way to perform photoluminescence measurements is to excite at E_{22} transition and measure the emission at E_{11}. However, the tunability range of our Ti:S laser (725nm - 995 nm) is not sufficient to address both E_{11} and E_{22} transitions. Therefore, we employed an alternative technique named phono-assisted photoluminescence excitation [188]. This method is based on the existence of phonon-assisted transition which are associated with the excitation of E_{11}. What we practically do is to excite nanotubes with energies that are higher than E_{11} and utilize the available phonon bands, namely the intermediate frequency modes [189], to excite E_{11} through phonon-relaxation process (Figure 7.10).

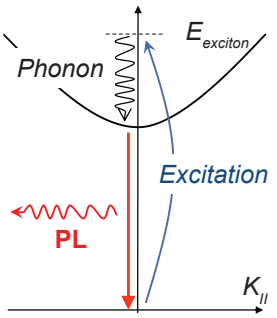

Figure 7.10: Schematic of phonon-assisted PL excitation. Figure adopted from [184].

In Figure 7.11 a typical example of a reflection/photoluminescence map is shown. The reflection map (Figure 7.11(a)), which is obtained with the secondary collection path, allows to accurately know the position of the laser beam on the sample, while it provides information about the surface. In Figure 7.11(c), a photoluminescence map which is obtained through the primary collection path, is illustrated. For each point of the map, the emission spectrum is recorded (Figure 7.11(b)). Such maps are very useful since they provide both spectral and spatial information on the optical emission of the surface of the sample, and therefore we are able to locate and characterize the optically active carbon nanotubes.

7.6.2 Nanotube diameter characterization

As it was mentioned earlier, one of the key requirement of this experiment is to systematically fabricate samples with high density of low diameter single-walled carbon nanotubes. It is well known that their density and diameter strongly depends on the CVD growth temperature [190, 191]. In order to optimize our growth process towards low diameter single-walled nanotubes, we investigated various growth temperatures. Figure 7.12 shows histograms of nanotubes measured at 2.8 K. Values are compared with literature ones in order to address chirality and diameter. We do not observe a clear trend in the diameter distribution when growth temperature goes from 830 to 900 °C. Nevertheless, significant fraction of sub-nanometer nanotubes are observed ((6,4) and (6,2)).

7.6.3 Excitons decoherence and stability

One of the key targets of this experiment is to obtain suspended carbon nanotubes that exhibit excitons with very low decoherence rate. In our samples we have successfully observe narrow linewidth emission from spatially localized excitons, but only in regions where the nanotubes are not suspended. Figure 7.13(a) shows the emission spectra of a carbon nanotube which emits at 893 nm, suggesting an (6,2) nanotube. We measured the optical linewidth using both of the available gratings (600 l/mm and 1200 l/mm) and each time we would get a linewidth close to the resolution limit of the corresponding grating ($\sim$ 150 μeV and $\sim$ 300 μeV), indicating that we are limited by the spectrometer resolution. This performance is comparable to recent observation of ultra narrow linewidth localized

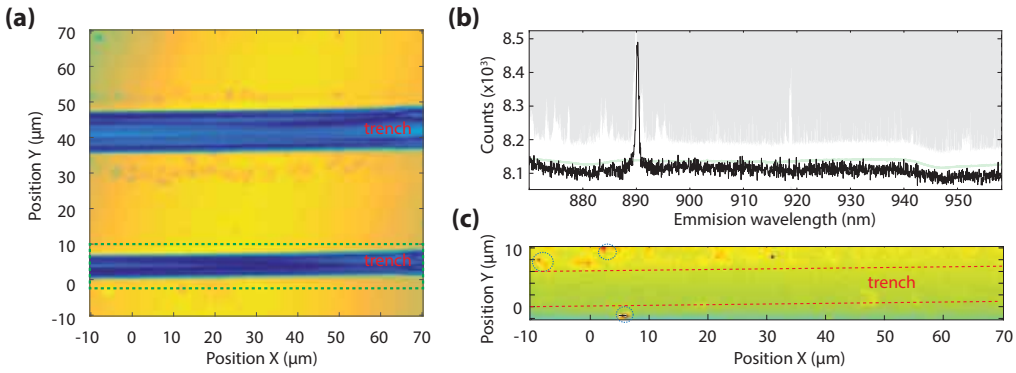

Figure 7.11: A typical example of reflection/PL map taken at 2.9 K. The wavelength of the excitation beam is at 800 nm, circularly polarized with 1.5 mW of power. **(a)** Reflection spatial color map of a sample acquired using the secondary collection path. X and Y axis correspond to position while the color scales with intensity of the reflected beam. The laser beam is focused on the surface of the sample. The trenches are depicted in the blue part of the image where the reflected light is less. **(b,c)** A photoluminescence map of the lower trench. Each point of the map correspond to a spectra acquired with the spectrometer. In (b), the emission spectra which corresponds to a specific point of the map is depicted, revealing a peak at 890 nm, arising from a nanotube that lies on the substrate. The emission spectra of all the map points, are plotted on the background with faint gray color. This reveal areas where tubes of different chiralities emit in different wavelengths. The color scale of the PL map that is shown at (c), corresponds to emission intensity at 890nm for each point on the map, revealing 3 points where emission at this wavelength appears. This allows to locate the various nanotubes on the map that emit in different wavelengths.

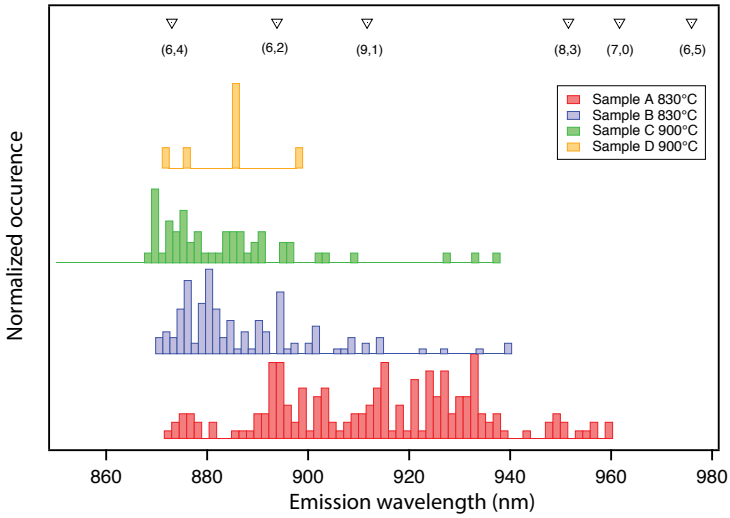

Figure 7.12: Chiralities statistics extracted from the photoluminescence emission measured at 2.8 K for carbon nanotubes samples that have grown in different temperatures. There has not been observed any strong dependence to temperature.

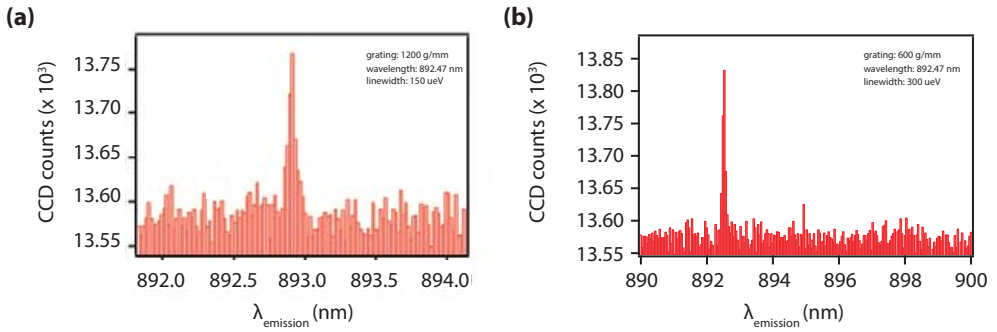

Figure 7.13: Exciton narrow linewidth emission. The optical linewidth is limited by the corresponding grating resolution. **(a)** Linewidth close to ($\sim$ 150 μeV at 900 nm) for the 1200 l/mm grating. **(b)** Linewidth close to ($\sim$ 300 μeV at 900 nm) for the 600 l/mm grating.

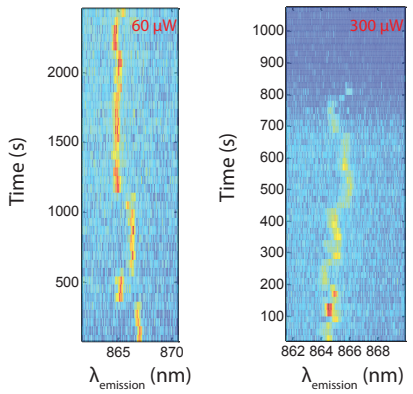

Figure 7.14: Time traces of photoluminescence emission from a nanotube for different excitation power at 4 K. At 60 μW (left), the PL spectra show considerably spectral wandering and blinking. At higher excitation power (300μW) spectral wondering and blinking increases before it quenches completely.

excitons in suspended nanotubes [166, 177]. In our experiment, we also attribute the low decoherence rate to excitons localization, however, the origin of the localization requires further investigation.

Another import parameter is the photoluminescence stability of carbon nanotubes. Figure 7.14 shows the emission spectra from another non suspended nanotube for different excitation power. Even in the lowest possible excitation power, where we can still detect a signal, there is considerable spectral wandering and blinking. In higher power the PL emission irreversibly quenches. This behavior constitutes a major hurdle for an optomechanics experiment and requires further investigation. It has been reported that PL stability can considerably increase in suspended nanotubes [166, 177].

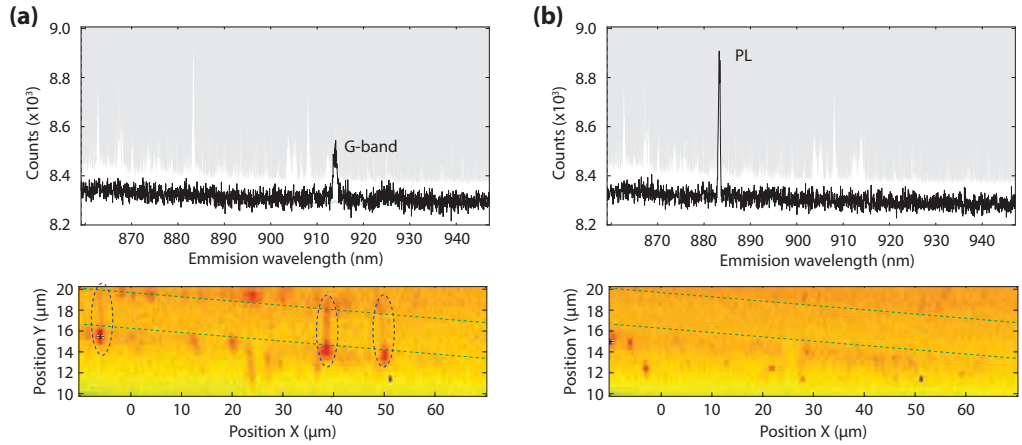

Figure 7.15: Photoluminescence map of a sample at 2.8 K with 1 mW circularly polarized 798nm laser beam excitation. **(a)** The color map (bottom figure) is calibrated according to the G-band Raman mode (top figure). Three tubes can be identified that are crossing the trench. **(b)** The color map (bottom figure) is calibrated according to the PL peak at 883 (top figure). There is no any carbon nanotube crossing the trench showing PL emission.

7.6.4 Photoluminescence quenching on suspended nanotubes

The biggest obstacle that we faced towards studying the excitons-phonons coupling in carbon nanotubes is that the PL emission from suspended nanotubes was a very rare event in our samples. The very few times that we succeeded to get emission from a suspended region of a nanotube, it was very unstable and irreversibly quenched after exposed for short amount of time under a very low excitation power. In Figure 7.15 a typical PL map of a sample is presented. While at least 3 suspended nanotubes show Raman scattering of the G-mode, non of them presents photoluminescence at any wavelength that is detectable with our setup.

The photoluminescence quenching of carbon nanotubes can be attributed to different mechanisms. As we stated earlier, excitons in a single-walled carbon nanotube decay non radiatively if the tube bundles with a metallic one. Indeed, SEM inspection reveal that there is a higher tendency for bundled tubes to be found suspended compared to individual tubes. Another reason may be related to the excessive excitation power that is used in order to overcome possible limited collection efficiency of our setup. As a result, the PL is quenched at the very beginning of each measurement. Finally, it is known that the PL efficiency of nanotubes is related to their environment. A non ideal vacuum of the chamber may lead to contamination of the nanotubes surface resulting in PL quenching.

7.7 Conclusions and outlook

In this chapter, we presented the first steps of a research effort towards studying the coupling between the motion of suspended single-walled carbon nanotubes and the localized zero-dimension excitons [166, 177] that exist in their structure. Suspended singly-walled

carbon nanotubes can be seen a hybrid nano-optomechanical system where the optical degrees of freedom are embedded inside their structure. For the purposes of this experiment we developed a low temperature micro-photoluminescence optical setup and a fabrication process for suspended single walled carbon nanotubes with low diameter. However, we faced various difficulties which prevented us from reaching our targeted goals in the time-frame of this Ph.D thesis. The main drawback is related to the difficulty to observe photoluminescence from carbon nanotubes that are suspended, preventing us from moving on the next step of studying the coupling to mechanical vibrations. The absence of photoluminescence can be attributed to various mechanisms with the most prominent to be the bundling between semiconducting and metallic nanotubes. Consequently, additional effort is required for the fabrication of high quality low diameter unbundled suspended tubes with high yield. Moreover, a further development of the optical setup, in order to improve the collection efficiency, will greatly facilitate this experiment.

Chapter 8

Conclusions

8.1 Summary

Over the course of this thesis we investigated a wide variety of different nanomechanical resonators based on graphene and carbon nanotubes, employing different transduction schemes and performing experiments from ambient to low temperatures.

In Chapter 5 we succeed to push the limits of modern nanofabrication techniques by realizing coupled graphene mechanical resonator devices for the first time. These complex all suspended structures consist of two graphene membranes coupled by a multi-walled carbon nanotube. We studied their dynamics at 4 K using frequency mixing techniques in order to fully characterizing their eigenmodes. Interestingly, even though the carbon nanotube introduces only a weak linear coupling between the two individual graphene resonators, in the high driving amplitude regime we observed nonlinear coupling between the eigenmodes of the system, highlighting the crucial role of nonlinearities at the ultimate one-dimensional and two-dimensional scaling limit of nanomechanics.

In Chapter 6 we switch our attention to even smaller systems by studying singly-clamped carbon nanotubes at room temperature. We were able to detect their noise dynamics with very high sensitivity by coupling their motion to the focused electron beam of a scanning electron microscope. This transduction scheme enabled us to extract the motion quadratures for each of the measured eigenmodes. We presented a detailed analysis of the two-dimensional noise trajectories both in space and time, and showed that such small objects behave as Brownian particles evolving in a two-dimensional harmonic potential. Moreover, we demonstrated phase-coherent measurements, which are central to the mechanical sensing [131], by implementing a phase-locked loop which allowed us to track the mechanical resonant frequency in real-time.

In Chapter 7 we presented the first steps of a research effort towards studying the coupling between the motion of suspended single-walled carbon nanotubes and their localized zero-dimension excitons [166, 177]. As grown carbon nanotubes can be seen as a hybrid nano-optomechanical system where the optical degrees of freedom are embedded inside the nanotube's structure. For the purposes of this experiment we developed a low temperature micro-photoluminescence optical setup and a fabrication process for long suspended single-walled carbon nanotubes with low diameter. We were able to observe narrow linewidth localized excitons from nanotubes that are found on the substrate, but we would rarely observe an optical response from suspended tubes, preventing us from

investigating optomechanical interactions. Although the final goals of this study were not reachable within the time-frame of this Ph.D thesis, plenty of useful knowledge was accumulated on the fabrication technologies, the optical properties of carbon nanotubes at low temperatures, and the experimental techniques that are required for such an experiment.

8.2 Outlook

Our work in Chapter 5 provided us considerable understanding on coupled low dimensional nanomechanical resonators. Nonetheless, there are plenty of intriguing phenomena to investigate in the future, including synchronization [98, 119], chaos [60], Landau-Zener transition [120], parametric mode splitting [99], coherent manipulation of phonon population [99, 121], and creation of mechanical 'dark' states [192]. In this direction, the progress in growth of graphene with chemically vapor deposition (CVD) [78] in addition to the advancements in two-dimensional materials transfer techniques [193] (see also Appendix D) allow for easy integration of graphene devices in a large scale. A possible extension on our work is to study coupled graphene resonators without using nanotubes as a coupling element, but shaping the suspended structure from on single piece of graphene. Such a technique will furthermore allow us to study systems with more than two coupled resonant elements.

In chapter 6 we made a significant progress on understanding the dynamics of carbon nanotube mechanical resonator at room temperature using a focused electron beam in order to detect their Brownian fluctuation in real-time. A next logical step is to use the same transduction scheme and methodology to investigate their dynamics at low temperatures in order to further shine light into their decoherence processes and explore novel thermodynamic regimes that were not accessible before. Additionally, by working in ultra high vacuum to avoid matter deposition from the electron beam, will allow us to perform mass and force sensing experiments with high sensitivity in real-time. A long term goal is that the above experiment can be possible combined with the objectives, methodologies and optical transduction techniques that we developed in Chapter 7. This would required further investigation on the fabrication side by better controlling the properties of the produces carbon nanotube resonators, as well as more detailed understanding on their exciton properties and the interaction of carbon nanotubes with light.

Our ultimate longterm vision is to achieve absolute control both on the fabrication of these nano-scale object, as well as on the detection and manipulation of their motion, reaching a point where we will be able to engineer complex, multifunctional, large-scale optoelectromechanical systems around graphene, carbon nanotubes, and other novel low-dimensional materials.

Appendix A

Theory of two coupled mechanical resonators

In this section we will develop the theoretical modelling in order to gain a better understanding on the dynamics of coupled graphene mechanical resonators that we study in chapter 5. We will closely follow the theoretical analysis and formalism on coupled nanomechanical resonators that are reported in Refs. [60, 117].

A system of two suspended graphene plates that are connected with a carbon nanotube, in a first approximation can be modeled as two resonators (graphene plates) that are coupled by an elastic spring (nanotube). We will first start by studying the coupling without including any nonlinearities in the equation of motion of each resonator. Then, we will study the behavior of coupled nonlinear resonators, as the structures that we experimentally investigated.

A.1 Coupling of two linear resonators

A system of two mechanical resonators, that are coupled by an elastic spring, can be modeled by introducing a linear coupling term $D(x_1 - x_2)$ in their equations of motion (3.5), where D is the coupling strength. Assuming equal masses, $m_1 = m_2 = m$, the dynamics of the coupled system will be then described by the following set of equations

$$m\ddot{x_1} + m\gamma_1\dot{x_1} + m(\omega_1^2 + D)x_1 - mDx_2 = F_1(t) \tag{A.1}$$

$$-mDx_1 + m\ddot{x_2} + m\gamma_2\dot{x_2} + m(\omega_2^2 + D)x_2 = F_2(t), \tag{A.2}$$

where x_1 and x_2 are the displacement, γ_1 and γ_2 the mechanical dissipation rate, and $F_1(t)$ and $F_2(t)$ the external driving force of each resonator.

The equation of motion for the whole system can be then expressed in a matrix form

$$M\ddot{\mathbf{x}} + \Gamma\dot{\mathbf{x}} + V\mathbf{x} = \mathbf{F}, \tag{A.3}$$

where $\mathbf{x} = (x_1, x_2)$ is a displacement vector and $\mathbf{F} = (F_1, F_2)$ is a vector of forces exerted on the individual resonators. M is the mass matrix, Γ is the damping matrix and V is

the potential matrix. These are given by

$$M = \begin{pmatrix} m & 0 \\ 0 & m \end{pmatrix} \tag{A.4}$$

$$\Gamma = \begin{pmatrix} m\gamma_1 & 0 \\ 0 & m_1\gamma_2 \end{pmatrix} = \begin{pmatrix} m\frac{\omega_1}{Q_1} & 0 \\ 0 & m\frac{\omega_2}{Q_2} \end{pmatrix} \tag{A.5}$$

$$V = \begin{pmatrix} m(\omega_1^2 + D) & -mD \\ -mD & m_2(\omega_2^2 + D) \end{pmatrix} \tag{A.6}$$

We assume that there is no damping ($\gamma_{1,2} = 0$) and no external driving force ($F_{1,2}(t) = 0$). In a normal mode, we assume all the masses oscillate at the same frequency, thus we try a harmonic solution on equation (A.3):

$$x_1(t) = x_{0,1}e^{i\omega t} \; and \; x_2(t) = x_{0,2}e^{i\omega t}. \tag{A.7}$$

and we get

$$-\omega^2 x_{0,1} + (\omega_1^2 + D)x_{0,1} - Dx_{0,2} = 0 \tag{A.8}$$

$$-Dx_{0,1} - \omega^2 x_{0,2} + (\omega_2^2 + D)x_{0,2} = 0. \tag{A.9}$$

These set of equations is a typical eigenvalue problem and is equivalent to diagonalizing the potential matrix V

$$\begin{pmatrix} m(\omega_1^2 + D) & -mD \\ -mD & m(\omega_2^2 + D) \end{pmatrix} \mathbf{x} = \omega_{I,II}^2 \mathbf{x}, \tag{A.10}$$

where the eigenvectors give the mode shapes and the eigenvalues ($\omega_{I,II}^2$) give the angular frequency of the eigenmodes. The determinant of $|V - \omega_{I,II}^2 I|$ should equal zero

$$\begin{vmatrix} \omega_1^2 + D + -\omega^2 & -D \\ -D & \omega_2^2 + D - \omega^2 \end{vmatrix} = 0. \tag{A.11}$$

The solution of (A.11) gives the eigenvalues

$$\omega_I^2 = \omega_m^2 + D - \sqrt{D^2 + \delta^2} \tag{A.12}$$

$$\omega_{II}^2 = \omega_m^2 + D + \sqrt{D^2 + \delta^2}, \tag{A.13}$$

where I and II denote the eigenmodes of the system. For convenience we introduced the mean frequency $\omega_m^2 = \frac{1}{2}(\omega_1^2 + \omega_2^2)$ and the detuning value $\delta = \frac{1}{2}(\omega_1^2 - \omega_2^2)$. The orthogonal normalized eigenvectors will be then given by

$$\mathbf{e_I} = \frac{1}{N_I}\begin{pmatrix} \frac{\delta + \sqrt{\delta^2 + D^2}}{D} \\ 1 \end{pmatrix}, \; \mathbf{e_{II}} = \frac{1}{N_{II}}\begin{pmatrix} \frac{\delta - \sqrt{\delta^2 + D^2}}{D} \\ 1 \end{pmatrix}, \tag{A.14}$$

where $N_I^2 = 1 + \frac{(\delta + \sqrt{\delta^2 + D^2})^2}{D^2}$ and $N_{II}^2 = 1 + \frac{(\delta - \sqrt{\delta^2 + D^2})^2}{D^2}$.

For $D = 0$ equations (A.12,A.13) describe a system of two independent resonators where the eigenfrequencies values correspond to their natural resonant frequencies (see Figure A.1(a))

$$\omega_I^2 = \omega_1^2 \tag{A.15}$$

$$\omega_{II}^2 = \omega_1^2 + 2\delta = \omega_2^2. \tag{A.16}$$

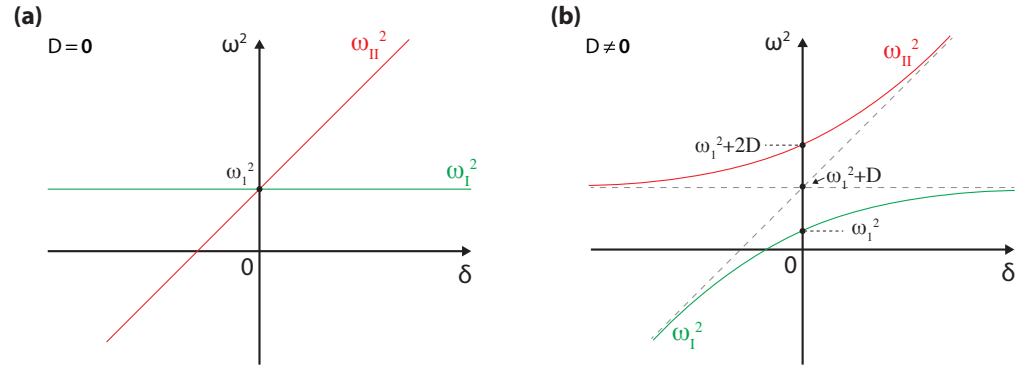

Figure A.1: Representation of the eigenmode frequencies versus detuning ($\delta = \frac{1}{2}(\omega_2^2 - \omega_1^2)$) for a sytem of two lineraly coupled resonators. **(a)** When the coupling equals zero ($D = 0$), it means that the two resonators can vibrate independendly in different frequencies. **(b)** When $D \neq 0$ and $\delta \approx 0$, a splitting of $\omega_{II}^2 - \omega_I^2 = 2D$ appears as an avoiding cross pattern in the eigenfrequencies versus detuning plot.

For $D \neq 0$, the solution of the above eigenvalues problem describes a system of two coupled resonators that has two independent eigenmodes (A.14) with two corresponding eigenfrequencies (A.12,A.13). Assuming that the two resonators are identical ($\delta = 0$), the first eigenmode is completely symmetric, with the two resonators vibrating in-phase with the same amplitude ($e_I = (1, 1)$) at an angular frequency which corresponds to the resonance frequency of each individual uncoupled resonator ($\omega_I = \omega_m = \omega_1 = \omega_2$). The second eigenmode is antisymmetric ($e_{II} = (-1, 1)$), meaning that the two resonators vibrate out of phase with the same amplitude, while its angular frequency is higher compared to the first eigenmode ($\omega_{II}^2 = \omega_I^2 + 2D$).

In the case of two individual resonators that are not identical ($\delta \neq 0$), the system still has an in-phase and an out of phase mode, but the amplitudes are not symmetric or antisymetric any more. The amplitude of the in-phase mode is mainly localized on the first resonator (the low frequency resonator), while the amplitude of the second eigenmode is mainly localized on the second mode. In the limit of $\delta \gg D$, the eigenfrequencies are given by:

$$\omega_I^2 \approx \omega_1^2 + D + \delta - |\delta| \tag{A.17}$$

$$\omega_{II}^2 \approx \omega_1^2 + D + \delta + |\delta|. \tag{A.18}$$

The behavior of eigenfrequencies versus detuning δ, for $D \neq 0$ is illustrated in Figure A.1(b), where a characteristic avoiding cross appears between the two eigenmodes when $\delta \approx 0$.

The diagonalization process of the potential matrix V, which is described above, results in the eigenmodes of the coupled system which are orthogonal. This allows as to treat the coupled system as two independed resonators. Following a dediagonalization procedure we can extract the new mass, damping and potential matrices. We define the conversion matrix as

$$A = \begin{pmatrix} \mathbf{e_{I,1}} & \mathbf{e_{II,1}} \\ \mathbf{e_{I,2}} & \mathbf{e_{II,2}} \end{pmatrix}, \tag{A.19}$$

where in the case of orthogonal eigenvectors, its transpose is equal the inverse, $A^T = A^{-1}$. By multiplying equation (A.3) with A^{-1} we get

$$M'\ddot{\mathbf{x}}' + \Gamma'\dot{\mathbf{x}}' + V'\mathbf{x}' = \mathbf{F}', \tag{A.20}$$

and the matrices will be then given by:

$$x' = A^T x,\ M' = A^T M A,\ \Gamma' = A^T \Gamma A,\ V' = A^T V A,\ F' = A^T F A. \tag{A.21}$$

As the eigenvectors are a result of a diagonalization process of V, V' is diagonal matrix. Also M' is a diagonal matrix, while damping the matrix Γ' has diagonal components if $\gamma_1 \neq \gamma_2$.

A.2 Coupling of two nonlinear resonators

In the previous section, we described a method to study the dynamics of two coupled resonators by introducing a linear coupling term. We extracted the eigenmodes and eigenfrequencies of such a system through a diagonalization process of the potential matrix V. However, we excluded any nonlinearities and external driving in the equation of motion.

To investigate a nonlinear system, we will employ secular perturbation theory [194]. In the limit of weak damping ($Q \gg 0$), a small expansion parameter $\epsilon = (Q_I Q_{II})^{-1/2}$ can be introduced, where Q_I and Q_{II} are the quality factors of the two eigenmodes. The physical parameters are then rescaled using two time scales: angular frequency $\omega = 1+\epsilon\Omega$, damping rate $\gamma_{1,2} = \epsilon\Gamma_{1,2}$, force $g_{D_{1,2}} = \epsilon^{3/2} g_{1,2}$ and time $t = \epsilon^{-1}T$. A system of two coupled equations of motion, where the masses are equal ($m_1 = m_2$), will be then written as

$$\begin{aligned} \ddot{x_1} + \gamma_1\dot{x_1} + \omega_1^2 x_1 + \alpha_1 x_1^3 + \eta_1 x_1^2\dot{x_1} + D(x_1 - x_2) &= g_{D_1}(t) \\ \ddot{x_2} + \gamma_2\dot{x_2} + \omega_2^2 x_2 + \alpha_2 x_2^3 + \eta_2 x_2^2\dot{x_2} + D(x_2 - x_1) &= g_{D_2}(t). \end{aligned} \tag{A.22}$$

The motion of the resonator away from equilibrium is expected to be on the order of $\epsilon^{1/2}$. Then the solution to this coupled nonlinear system, as expressed by modal eigenvectors (see equation A.21), is given by

$$\mathbf{x} = \frac{\sqrt{\epsilon}}{2}[A_I(T)e^{i\omega_I t}\mathbf{e_I} + A_{II}(T)e^{i\omega_{II} t}\mathbf{e_{II}} + c.c.] + e^{3/2}\mathbf{x}^{(1)}(t) + \dots\ , \tag{A.23}$$

where the two-dimensional vectors are indicated with bold font; the components of $\mathbf{x}$ are the displacement of each resonator $(x_{0,1}, x_{0,2})$, $\mathbf{e_I} = (e_{I,1}, e_{I,2})$ and $\mathbf{e_{II}} = (e_{II,2}, e_{II,2})$ are the eigenvectors representing the mode shapes, and $\mathbf{x}^{(1)}(t)$ is a vector of next order corrections.

The forces that are driving each individual resonator, which appear in the coupled equation of motion (A.22), are given by $g_{D_{1,2}} = \epsilon^{3/2} g_{1,2}$. In the most general case, where each resonator can be independently actuated in both resonant frequencies simultaneously, the scaled forces are given by

$$\begin{aligned} g_1(t) &= \frac{1}{2}[g_{1,I}(T)e^{i\omega_I t} + g_{1,II}(T)e^{i\omega_{II} t} + c.c.] \\ g_2(t) &= \frac{1}{2}[g_{2,I}(T)e^{i\omega_I t} + g_{2,II}(T)e^{i\omega_{II} t} + c.c.], \end{aligned} \tag{A.24}$$

where $g_{i,j}(T)$ [1] indicates the part of the driving force exerted upon the i^{th} resonator near the resonance frequency of mode j. If the driving force frequency is offset to the corresponding resonant frequency, $\omega_{Dj} = \omega_j + \epsilon\Omega_j$, then the expression for the force has the form $g_{i,j}(T) = |g_{i,j}(T)|e^{i\Omega_j T}$.

Starting from equation (A.23), it is also possible to calculate $\dot{x}_{0,i}(t)$, $\ddot{x}_{0,i}(t)$, $x^3_{0,i}(t)$, $x^2_{0,i}(t), \ddot{x}_{0,i}(t)$. After substituting those quantities and equations (A.23,A.24) into equation (A.22), it can be shown that the equation of motion takes the form:

$$\begin{aligned}
&\begin{pmatrix} -\frac{d^2}{dt^2} - \omega_1^2 - D & D \\ D & -\frac{d^2}{dt^2} - \omega_2^2 - D \end{pmatrix} \mathbf{x^{(1)}} = e^{i\omega_I t}\Bigg[i\omega_I A_I' \begin{pmatrix} e_{I,1} \\ e_{I,2} \end{pmatrix} + \frac{i\omega_I}{2} A_I \begin{pmatrix} \Gamma_1 e_{I,1} \\ \Gamma_2 e_{I,2} \end{pmatrix} \\
&+ \frac{3}{8}|A_I|^2 A_I \begin{pmatrix} \alpha_1 e_{I,1}^3 \\ \alpha_2 e_{I,2}^3 \end{pmatrix} + \frac{3}{4}|A_{II}|^2 A_I \begin{pmatrix} \alpha_1 e_{I,1}\ e_{II,1}^2 \\ \alpha_2 e_{I,1}\ e_{II,2}^2 \end{pmatrix} + i\frac{1}{8}\omega_I |A_I|^2 A_I \begin{pmatrix} \eta_1 e_{I,1}^3 \\ \eta_2 e_{I,2}^3 \end{pmatrix} \\
&+ i\frac{1}{4}\omega_I |A_{II}|^2 A_I \begin{pmatrix} \eta_1 e_{I,1}\ e_{II,1}^2 \\ \eta_2 e_{I,1}\ e_{II,2}^2 \end{pmatrix} - \frac{1}{2}\begin{pmatrix} g_{1,I} \\ g_{2,I} \end{pmatrix} + c.c. \Bigg] + e^{i\omega_{II}t}[...] + e^{-i\omega_{II}t}[...] \\
&+ \ nonresonant\ terms,
\end{aligned} \tag{A.25}$$

where $\Gamma_i = \epsilon^{-1}\gamma_i$ are the scaled damping parameters for each resonator, and A_I' the derivative of the first eigenmode amplitude with respect to the slow time T.

The left hand side of equation (A.25) represents a system of two resonators with no damping. Therefore, the right hand side terms that are time-varying at ω_I and ω_{II} must be orthogonal to eigenvectors $\mathbf{e_I}$ and $\mathbf{e_{II}}$ respectively. Following this requirement, we can extract the secular equations of motion for the amplitudes of each eigenmode, A_I and A_{II}. For $\|\mathbf{e_{II}}\| = \|\mathbf{e_I}\| = 0$, A_I is given by

$$\begin{aligned}
&i\omega_I A_I' + i\frac{\omega_I}{2} A_I(\Gamma_1 e_{I,1}^2 + \Gamma_2 e_{I,2}^2) + \frac{3}{8}|A_I|^2 A_I(\alpha_1 e_{I,1}^4 + \alpha_2 e_{I,2}^4) \\
&+ \frac{3}{4}|A_{II}|^2 A_I(\alpha_1 e_{I,1}^2 \epsilon_{II,1}^2 + \alpha_2 e_{I,2}^2 e_{II,2}^2) \\
&+ i\frac{\omega_I}{8}|A_I|^2 A_I(\eta_1 e_{I,1}^4 + \eta_2 e_{I,2}^4) + i\frac{\omega_I}{4}|A_{II}^2|A_I(\eta_1 e_{I,1}^2 e_{II,1}^2 + \eta_2 e_{I,2}^2 e_{II,2}^2) \\
&= \frac{1}{2}(g_{1,I} e_{I,1} + g_{2,I} e_{I,2}),
\end{aligned} \tag{A.26}$$

and A_{II} by

$$\begin{aligned}
&i\omega_{II} A_{II}' + i\frac{\omega_{II}}{2} A_{II}(\Gamma_1 e_{II,1}^2 + \Gamma_2 e_{II,2}^2) + \frac{3}{8}|A_{II}|^2 A_{II}(\alpha_1 e_{II,1}^4 + \alpha_2 e_{II,2}^4) \\
&+ \frac{3}{4}|A_I|^2 A_{II}(\alpha_1 e_{II,1}^2 \epsilon_{I,1}^2 + \alpha_2 e_{II,2}^2 e_{I,2}^2) \\
&+ i\frac{\omega_{II}}{8}|A_{II}|^2 A_{II}(\eta_1 e_{II,1}^4 + \eta_2 e_{II,2}^4) + i\frac{\omega_{II}}{4}|A_I^2|A_{II}(\eta_1 e_{II,1}^2 e_{I,1}^2 + \eta_2 e_{II,2}^2 e_{I,2}^2) \\
&= \frac{1}{2}(g_{1,II} e_{II,1} + g_{2,II} e_{II,2}),
\end{aligned} \tag{A.27}$$

[1] Where i denotes the number of the individual resonator and j the number of the eigenmode.

where only the resonant terms of each eigenmode are kept. These two secular equations can be rewritten in the following form:

$$\begin{aligned} i\omega_I \frac{dA_I}{dT} + i\omega\Gamma_I A_I + \alpha_I |A_I|^2 A_I + \beta_I |A_{II}|^2 A_I \\ + i\omega_I(\xi_I |A_I|^2 A_I + \Psi_I |A_{II}|^2 A_I) = G_I(t) \\ i\omega_{II} \frac{dA_{II}}{dT} + i\omega\Gamma_{II} A_{II} + \alpha_{II} |A_{II}|^2 A_{II} + \beta_{II} |A_I|^2 A_{II} \\ + i\omega_{II}(\xi_{II} |A_{II}|^2 A_{II} + \Psi_{II} |A_I|^2 A_{II}) = G_{II}(t), \end{aligned} \tag{A.28}$$

where for mode I:

$$\begin{aligned} \Gamma_I &= \frac{1}{2}[\Gamma_1 e_{I,1}^2 + \Gamma_2 e_{I,2}^2] \\ \alpha_I &= \frac{3}{8}[\alpha_1 e_{I,1}^4 + \alpha_2 e_{I,2}^4] \\ \beta_I &= \frac{3}{4}[\alpha_1 e_{I,1}^2 e_{II,1}^2 + \alpha_2 e_{I,2}^2 e_{II,2}^2] \\ \xi_I &= \frac{1}{8}[\eta_1 e_{I,1}^4 + \eta_2 e_{I,2}^4] \\ \Psi_I &= \frac{1}{4}[\eta_1 e_{I,1}^2 e_{II,2}^2 + \eta_2 e_{I,2}^2 e_{II,2}^2] \\ G_I &= \frac{1}{2}[g_{1,I} e_{I,1} + g_{2,I} e_{I,2}], \end{aligned} \tag{A.29}$$

and equivalently for mode II:

$$\begin{aligned} \Gamma_{II} &= \frac{1}{2}[\Gamma_1 e_{II,1}^2 + \Gamma_2 e_{II,2}^2] \\ \alpha_{II} &= \frac{3}{8}[\alpha_1 e_{II,1}^4 + \alpha_2 e_{II,2}^4] \\ \beta_{II} &= \frac{3}{4}[\alpha_1 e_{I,1}^2 e_{II,1}^2 + \alpha_2 e_{I,2}^2 e_{II,2}^2] \\ \xi_{II} &= \frac{1}{8}[\eta_1 e_{II,1}^4 + \eta_2 e_{II,2}^4] \\ \Psi_{II} &= \frac{1}{4}[\eta_1 e_{II,1}^2 e_{I,2}^2 + \eta_2 e_{II,2}^2 e_{I,2}^2] \\ G_{II} &= \frac{1}{2}[g_{1,II} e_{II,1} + g_{2,II} e_{II,2}]. \end{aligned} \tag{A.30}$$

When the eigenmodes are driven near their resonant frequencies with frequency shift $\Omega_{I,II}$, so that $G_{I,II}(T) = |G_{I,II}|e^{i\Omega_{I,II}T}$, the eigenmode amplitudes will be given by $A_{I,II}(T) = |A_{I,II}|e^{i\Omega_{I,II}T}$. The stationary solution for the set of equations (A.29) will be given by

$$\begin{aligned} |A_I|^2 &= \frac{|G_I|^2}{\omega_I^2} \frac{1}{(\Omega_I - \alpha_I |A_I|^2 - \beta_I |A_{II}|^2)^2 + (\Gamma_I + \xi_I |A_I|^2 + \Psi_I |A_{II}|^2)^2} \\ |A_{II}|^2 &= \frac{|G_{II}|^2}{\omega_{II}^2} \frac{1}{(\Omega_{II} - \alpha_{II} |A_{II}|^2 - \beta_{II} |A_I|^2)^2 + (\Gamma_{II} + \xi_{II} |A_{II}|^2 + \Psi_{II} |A_I|^2)^2}. \end{aligned} \tag{A.31}$$

Equation (A.31) predicts some very interesting phenomena that appear in a system of two coupled nonlinear mechanical resonators. Assuming that there is no nonlinear dumping ($\Psi_{I,II} = 0, \xi_{I,II} = 0$), if mode I is driven in the linear regime, meaning that $|A_I|^2$ is small and $\alpha_I|A_I|^2 \ll \beta_I|A_{II}|^2$, and if mode II is driven in the nonlinear regime, then the resonance frequency of mode I varies like the square amplitude of mode II. Essentially the frequency of mode I can be tuned by controlling the amplitude of mode II. This frequency pulling effect appears due to the nonlinearities that exist in the equation of motion of each individual resonator, even though their coupling is modeled by just a linear term D. [2]

[2] This effect should not be confused with the mode splitting due to the strong linear coupling that is described in the previous section.

Appendix B

Quadratures of motion

B.1 Concept

A convenient way to describe a periodic signal $a(t) = A(t)\cos((\omega t) + \phi(t))$ is to express it in a rotating frame at the oscillating frequency ω. It will then take the following form:

$$a(t) = I(t)\ \cos(\omega t) + Q(t)\ \sin(\omega t), \tag{B.1}$$

where $I(t)$ and $Q(t)$ are time-varying amplitudes, the so-called quadratures of signal $a(t)$. To study the motion $x(t)$ of a mechanical resonator, it is preferable to work in the rotating frame of its mechanical resonant frequency ω_0 [141]. The amplitude of motion will be then given by

$$x(t) = X_1(t)\ \cos(\omega_0 t) + X_2(t)\ \sin(\omega_0 t), \tag{B.2}$$

where $X_1(t)$ is the in-phase quadrature and $X_2(t)$ the out of phase quadrature of motion. This formalism allows to study the evolution of a mechanical resonator in the phase space, using only the slowly-varying in time components $X_1(t)$ and $X_2(t)$ (their time scales are above $1/\gamma_m$) and removing the intrinsic oscillatory dependence with time at ω_0. Experimentally it is more convenient to work with the low frequency signal of the quadrature components ($\leq \gamma_m$), due to the low bandwidth requirements compared to a signal at the mechanical resonant frequency ($\gamma_{\mathrm{m}} \ll \omega_0$).

In the frequency space the Fourier components of the quadratures can be written as [141]

$$\begin{aligned} X_1(\omega) &= x(\omega_0 + \omega) + x(-\omega_0 + \omega), \\ X_2(\omega) &= -i(x(\omega_0 + \omega) - x(-\omega_0 + \omega)), \end{aligned} \tag{B.3}$$

where $\omega = \omega_a - \omega_0$ is the frequency missmatch between the analysis frequency ω_a and the mechanical resonant frequency ω_0, and is always considered small compared to ω_0.

From equation (3.7) and (3.8) by inserting the expressions of $x(\omega_0+\omega)$ and $x(-\omega_0+\omega)$ in the definitions of $X_1(\omega)$ and $X_2(\omega)$, we can extract the quadratures in presence of

applied force:

$$X_1(\omega) = -\frac{1}{2m\omega_0}\left(\frac{1}{-i\omega+\gamma/2}\right)F_2(\omega),$$
$$X_2(\omega) = \frac{1}{2m\omega_0}\left(\frac{1}{-i\omega+\gamma/2}\right)F_1(\omega), \tag{B.4}$$

where $F_1(\omega)$ and $F_2(\omega)$ correspond to the two quadratures of the applied force defined in the Fourier space.

In [195] it has been shown that the autocorrelation function of the thermal force F^{th} as expressed in the quadrature frame is given by

$$\langle F_1^{\mathrm{th}(\omega)} F_1^{\mathrm{th}(\omega')}\rangle = \langle F_2^{\mathrm{th}(\omega)} F_2^{\mathrm{th}(\omega')}\rangle = 4m_{\mathrm{eff}}\gamma_m k_B T 2\pi\delta(\omega+\omega'). \tag{B.5}$$

The double sideband power spectral density of F_1 and F_2 is frequency independed and is given by

$$S^{\mathrm{th}}_{F_1F_1} = S^{\mathrm{th}}_{F_2F_2} = 4m_{\mathrm{eff}}\gamma_m k_B T = 2S^{\mathrm{th}}_F. \tag{B.6}$$

Using equation (B.4) we can then extract the double sided displacement spectral density of each quadrature:

$$S^{\mathrm{th}}_{X_1X_1}(\omega) = S^{\mathrm{th}}_{X_2X_2}(\omega) = \frac{\gamma_m k_B T}{m_{\mathrm{eff}}\omega_0^2(\omega^2+\gamma_m^2/4)}. \tag{B.7}$$

The integral of the single sided power spectral density of each quadrature will be given by

$$\langle X_1^2\rangle = \langle X_2^2\rangle = \frac{k_B T}{m_{\mathrm{eff}}\omega_0^2} = \langle x_{\mathrm{th}}\rangle. \tag{B.8}$$

As we can see, this result is equal as the one we obtained for an integration of the displacement spectrum of the trajectory $x(t)$ in the standard frame.

The temporal correlation function of the quadratures is defined as $C_{ij} = \langle X_i(t)X_i(t+\tau)\rangle$, where i and j give the indices of the quadratures and $\langle ...\rangle$ denotes statistical averaging. It can be shown that [141]:

$$C_{12}(\tau) = C_{21}(\tau) = 0 \tag{B.9}$$
$$C_{ii}(\tau) = \langle X_i^2\rangle e^{-\frac{\gamma_m\tau}{2}}. \tag{B.10}$$

The last expression the amplitude of the autocorrelation function exponentially decays with a decay rate given by the half of the mechanical dissipation.

B.2 Quadratures demodulation

The experimental principles of quadratures demodulation, as implemented for the experiments that are presented in chapter 6, are depicted in Figure B.1. The electromechanical

fluctuations signal $x(t)$ at the output of the secondary electrons detector [1] is splitted into two branches. Each branch is mixed with the in-phase ($\cos\omega_{\mathrm{d}}t$) and the out of phase signal ($\sin\omega_{\mathrm{d}}t$) of the same local oscillator at the demodulation frequency ω_{d}:

$$\tilde{I}(t) = x(t) \times \cos\omega_{\mathrm{d}}t \tag{B.11}$$

$$\tilde{Q}(t) = x(t) \times \sin\omega_{\mathrm{d}}t. \tag{B.12}$$

Assuming that there is a detuning between the demodulation frequency and the actual mechanical resonant frequency ($\omega_{\mathrm{d}} \neq \omega_0$), the measured quadratures can be expressed in terms of the intrinsic mechanical quadratures $X_1(t)$ and $X_2(t)$, as they are defined in equation (B.2),

$$\begin{aligned}\tilde{I}(t) &= \frac{1}{2}[\cos(\omega_0-\omega_{\mathrm{d}})t + \cos(\omega_0+\omega_{\mathrm{d}})t]X_1(t) + \frac{1}{2}[\sin(\omega_0+\omega_{\mathrm{d}})t + \sin(\omega_0-\omega_{\mathrm{d}})t]X_2(t)\\ \tilde{Q}(t) &= \frac{1}{2}[\sin(\omega_0+\omega_{\mathrm{d}})t - \sin(\omega_0-\omega_{\mathrm{d}})t]X_1(t) + \frac{1}{2}[\cos(\omega_0-\omega_{\mathrm{d}})t - \cos(\omega_0-\omega_{\mathrm{d}})t]X_2(t).\end{aligned} \tag{B.13}$$

A low-pass filter is applied in each branch to suppress the high frequency component and leaving only the slowly varying signal at baseband frequencies. Assuming that $|\omega_0-\omega_{\mathrm{d}}| \ll \omega_m$, the previous expressions can be simplified to

$$\begin{aligned}I(t) = (F * \tilde{I})(t) &= \frac{1}{2}X_1(t)\cos(\omega_0-\omega_{\mathrm{d}})t + \frac{1}{2}X_2(t)\sin(\omega_0-\omega_{\mathrm{d}})t\\ Q(t) = (F * \tilde{Q})(t) &= -\frac{1}{2}X_1(t)\sin(\omega_0-\omega_{\mathrm{d}})t + \frac{1}{2}X_2(t)\cos(\omega_0-\omega_{\mathrm{d}})t,\end{aligned} \tag{B.14}$$

where F denotes low-pass filtering convolution. $I(t)$ and $Q(t)$ express the quadratures of motion in a referential rotating frame of the demodulation frequency ω_{d}, which is detuned by $\Delta\omega = |\omega_0 - \omega_{\mathrm{d}}|$ from the actual mechanical resonant frequency at ω_0. The above expression can be expressed in a matrix form

$$\begin{bmatrix} I(t) \\ Q(t) \end{bmatrix} = \frac{1}{2}\begin{bmatrix} \cos(\omega_0-\omega_{\mathrm{d}})t & \sin(\omega_0-\omega_{\mathrm{d}})t \\ -\sin(\omega_0-\omega_{\mathrm{d}})t & \cos(\omega_0-\omega_{\mathrm{d}})t \end{bmatrix}\begin{bmatrix} X_1(t) \\ X_2(t) \end{bmatrix} \tag{B.15}$$

$$\Rightarrow \begin{bmatrix} I(t) \\ Q(t) \end{bmatrix} = R^{\mathrm{T}}\begin{bmatrix} X_1(t) \\ X_2(t) \end{bmatrix}, \tag{B.16}$$

where R^{T} is the transpose of the rotation matrix

$$R = \begin{bmatrix} \cos(\omega_0-\omega_{\mathrm{d}})t & -\sin(\omega_0-\omega_{\mathrm{d}})t \\ \sin(\omega_0-\omega_{\mathrm{d}})t & \cos(\omega_0-\omega_{\mathrm{d}})t \end{bmatrix}.$$

For a rotation matrix it holds true that $R^{\mathrm{T}} = R^{-1}$, thus the intrinsic quadratures will be given by

$$\begin{bmatrix} X_1(t) \\ X_2(t) \end{bmatrix} = \begin{bmatrix} (\tilde{X}_1 * F)(t) \\ (\tilde{X}_2 * F)(t) \end{bmatrix} = 2\begin{bmatrix} \cos(\omega_0-\omega_{\mathrm{d}})t & -\sin(\omega_0-\omega_{\mathrm{d}})t \\ \sin(\omega_0-\omega_{\mathrm{d}})t & \cos(\omega_0-\omega_{\mathrm{d}})t \end{bmatrix}\begin{bmatrix} I(t) \\ Q(t) \end{bmatrix}, \tag{B.17}$$

[1] Depending on the available bandwidth, the quadratures demodulation technique principles can be applied in conjunction to other transduction schemes, like the electro-optomechanical signal that comes out of a photodiode in optical transduction schemes, or the electromechanical signal in the direct electrical readout.

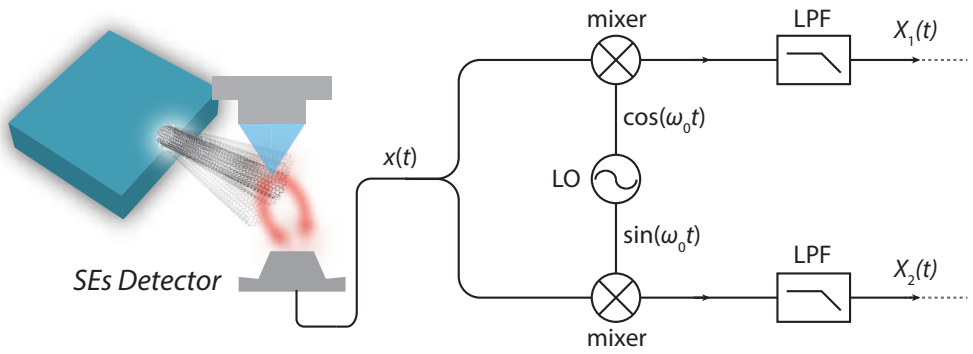

Figure B.1: Quadratures demodulation scheme as used in chapter 6. The electromechanical signal $x(t)$ at the output of the secondary electrons detector is splitted into two different branches. The one branch is mixed with the in-phase signal of a local oscillator ($\cos(\omega_d t)$) and the other branch with a out of phase shifted signal of the same local oscillator ($\sin(\omega_d t)$). The demodulation frequency ideally is selected to be the frequency of the mechanical mode of interest ($\omega_d = \omega_0$). The mixing process will create components at baseband frequencies (DC) and at higher frequencies. The slowly-varying in time $X_1(t)$ and $X_2(t)$ components are extracted with a low pass filter at the output of each branch, that removes the high frequency and keep only the baseband frequency mixing components.

where the factor 2 can be seen as a scaling parameter depending on the relative amplitude of the local oscillator reference signal that was used for the mixing process. Starting from equation (B.2) and using (B.17), it can be shown that

$$x(t) = 2I(t)\cos\omega_{\mathrm{d}}t + 2Q(t)\sin\omega_{\mathrm{d}}t. \tag{B.18}$$

An alternative and convenient way to represent the quadratures of motion, and perform all the necessary signal processing, is to use complex numbers. The electromechanical signal will be given by

$$x(t) = \Re((X_1(t) + iX_2(t))e^{-i\omega_0 t}) = X_1(t)\cos\omega_0 t + X_2(t)\sin\omega_0 t. \tag{B.19}$$

The demodulation process will be described by

$$\begin{aligned}\tilde{x}(t) = (x(t)e^{i\omega_{\mathrm{d}}t}) * F) = \frac{1}{2}X_1(t)e^{-i(\omega_0-\omega_{\mathrm{d}})t} + i\frac{1}{2}X_2(t)e^{-i(\omega_0-\omega_{\mathrm{d}})t} = \\ \Big[\frac{1}{2}[X_1(t)\cos(\omega_0-\omega_{\mathrm{d}}t) + X_1(t)\sin(\omega_0-\omega_{\mathrm{d}}t)]\Big] + \\ i[\frac{1}{2}[-X_1(t)\sin(\omega_0-\omega_{\mathrm{d}}t) + X_2(t)\cos(\omega_0-\omega_{\mathrm{d}}t)],\end{aligned} \tag{B.20}$$

where $I(t) = \Re(\tilde{x}(t))$ and $Q(t) = \Im(\tilde{x}(t))$ are the demodulated quadratures at a referential rotating framing of ω_{d}, expressed in the real mechanical quadratures as we have seen before.

A perfect demodulation of the electromechanical signal $x(t)$ is achieved when $\omega_{\mathrm{d}} = \omega_0$,

resulting into the extraction of the intrinsic quadratures of the mechanical trajectory

$$\begin{aligned} X_1(t) &= \frac{1}{2} I(t) \\ X_2(t) &= \frac{1}{2} Q(t). \end{aligned} \tag{B.21}$$

Appendix C

Energy autocorrelation function of a noise driven harmonic oscillator

C.1 Single-mode energy autocorrelation

In this section, we derive the expression of the energy autocorrelation function $C_{\mathcal{E}}(t, t+\tau) = \langle \mathcal{E}(t)\mathcal{E}(t+\tau)\rangle$, with $\mathcal{E}(t) = X_1^2(t) + X_2^2(t)$ the mechanical energy, $X_{1,2}(t)$ the motion quadratures, and where $\langle ...\rangle$ denotes statistical averaging over the driving external bath. In the following, we will assume the mechanical oscillator to be driven by a stationary, Gaussian bath.

We start with calculating the second moment autocorrelation function $C_{X^2}(t, t+\tau) = \langle X^2(t)X^2(t+\tau)\rangle$ associated with one given quadrature X (the mechanical motion being assumed to be driven by a Gaussian noise, this expression will be identical for any given motion quadrature). For a high-Q harmonic oscillator, the time evolution of such quadrature corresponds to the convolution between the quadrature impulse response $\chi(t)$ and an effective Gaussian driving noise $F_X^{th}(t)$ such that $\langle F_X^{th}(t)F_X^{th}(t') = 2S_F^{th}\delta(t'-t)\rangle$ (S_F^{th} the single sideband force spectral density associated with the external driving bath, and $\hat{\text{I}}\text{t}$ the Dirac delta function)

$$X(t) = \int_{-\infty}^{+\infty} \mathrm{d}t_1 \chi(t-t_1) F_X^{\mathrm{th}}(t_1) \tag{C.1}$$

$$\chi(t) = \frac{1}{2m_{\mathrm{eff}}\omega_0}\Theta(t)e^{-\frac{\gamma_{\mathrm{m}}}{2}t}, \tag{C.2}$$

with m_{eff}, ω_0, and γ_{m} the mass, mechanical resonant frequency and the mechanical damping rate of the oscillator, and with Θ denoting the Heaviside step function. Assuming the stationary nature of the problem, all correlation functions are time independent, $C_{X^2}(t, t+\tau) = C_{X^2}(0, \tau) = C_{X^2}(\tau)$. Using equations (C.1) and (C.2), this autocorrela-

tion function can be subsequently expanded as

$$\begin{aligned}
C_{X^2}(\tau) &= \langle X^2(0)X^2(\tau)\rangle \\
&= \langle \left(\int_{-\infty}^{+\infty} \mathrm{d}t_1 \chi(-t_1) F_X^{\mathrm{th}}(t_1) \right)^2 \left(\int_{-\infty}^{+\infty} \mathrm{d}t_2 \chi(\tau - t_2) F_X^{\mathrm{th}}(t_2) \right)^2 \rangle \\
&= \langle \int\int\int\int_{[-\infty,+\infty]^4} \mathrm{d}t_1 \mathrm{d}t_2 \mathrm{d}t_3 \mathrm{d}t_4 \chi(-t_1 \chi(-t_2) \chi(\tau - t_3) \chi(\tau - t_4) F_X^{\mathrm{th}}(t_1) F_X^{\mathrm{th}}(t_2) F_X^{\mathrm{th}}(t_3) F_X^{\mathrm{th}}(t_4) \rangle \\
&= \int\int\int\int_{[-\infty,+\infty]^4} \mathrm{d}t_1 \mathrm{d}t_2 \mathrm{d}t_3 \mathrm{d}t_4 \chi(-t_1 \chi(-t_2) \chi(\tau - t_3) \chi(\tau - t_4) \langle F_X^{\mathrm{th}}(t_1) F_X^{\mathrm{th}}(t_2) F_X^{\mathrm{th}}(t_3) F_X^{\mathrm{th}}(t_4) \rangle,
\end{aligned} \tag{C.3}$$

where the integral and the statistical average have been swapped between the third and last steps because of the stationarity of the problem. To determine the value of the quadruplet $\langle F_X^{\mathrm{th}}(t_1) F_X^{\mathrm{th}}(t_2) F_X^{\mathrm{th}}(t_3) F_X^{\mathrm{th}}(t_4) \rangle$, we use Wick's theorem [1], which states that it can be rewritten as the sum of all possible binomial contractions of its components:

$$\begin{aligned}
\langle F_X^{\mathrm{th}}(t_1) F_X^{\mathrm{th}}(t_2) F_X^{\mathrm{th}}(t_3) F_X^{\mathrm{th}}(t_4) \rangle = {} & \langle F_X^{\mathrm{th}}(t_1) F_X^{\mathrm{th}}(t_2) \rangle \langle F_X^{\mathrm{th}}(t_3) F_X^{\mathrm{th}}(t_4) \rangle + \\
& \langle F_X^{\mathrm{th}}(t_1) F_X^{\mathrm{th}}(t_3) \rangle \langle F_X^{\mathrm{th}}(t_2) F_X^{\mathrm{th}}(t_4) \rangle + \\
& \langle F_X^{\mathrm{th}}(t_1) F_X^{\mathrm{th}}(t_4) \rangle \langle F_X^{\mathrm{th}}(t_2) F_X^{\mathrm{th}}(t_3) \rangle.
\end{aligned} \tag{C.4}$$

Using that $\langle F_X^{\mathrm{th}}(t) F_X^{\mathrm{th}}(t') = 2 S_{\mathrm{F}}^{\mathrm{th}} \delta(t' - t) \rangle$, we finally obtain:

$$\begin{aligned}
C_{X^2}(\tau) = {} & 4 (S_{\mathrm{F}}^{\mathrm{th}})^2 \int\int\int\int_{[-\infty,+\infty]^4} \mathrm{d}t_1 \mathrm{d}t_2 \mathrm{d}t_3 \mathrm{d}t_4 \times \\
& (\delta(t_2 - t_1)\delta(t_4 - t_3) + \delta(t_3 - t_1)\delta(t_4 - t_2) + \delta(t_4 - t_1)\delta(t_3 - t_2)).
\end{aligned} \tag{C.5}$$

It is therefore straight to simplify equation (C.5) to obtain:

$$\frac{1}{4(S_{\mathrm{F}}^{\mathrm{th}})^2} C_{X^2}(\tau) = \int\int_{[-\infty,+\infty]^2} \mathrm{d}t_1 \mathrm{d}t_3 \chi^2(-t_1) \chi^2(\tau - t_3) + 2 \left(\int_{-\infty}^{+\infty} \mathrm{d}t_1 \chi(-t_1) \chi(\tau - t_1) \right)^2. \tag{C.6}$$

The two terms on the right side of equation (C.6) can be straight forward computed:

$$\int\int_{[-\infty,+\infty]^2} \mathrm{d}t_1 \mathrm{d}t_3 \chi^2(-t_1) \chi^2(\tau - t_3) = \left(\frac{1}{2 m_{\mathrm{eff}} \omega_0} \right)^4 \times \frac{1}{\gamma_{\mathrm{m}}^2}, \tag{C.7}$$

$$\left(\int_{-\infty}^{+\infty} \mathrm{d}t_1 \chi(-t_1) \chi(\tau - t_1) \right)^2 = \left(\frac{1}{2 m_{eff} \omega_0} \right)^4 \times \frac{1}{\gamma_{\mathrm{m}}^2} e^{-\gamma_{\mathrm{m}} |\tau|}, \tag{C.8}$$

[1] Indeed, Wick's theorem applies, F_X^{th} being a Gaussian, centered statistical variable.

and finally:

$$C_{X^2}(\tau) = 4\left(\frac{1}{2m_{eff}\omega_0}\right)^4\left(\frac{S_F^{th}}{\gamma_m}\right)\left(1+2e^{-\gamma_m|\tau|}\right). \tag{C.9}$$

We now resume and terminate the calculation of the energy autocorrelation function $C_{\mathcal{E}}(\tau) = C_{\mathcal{E}}(0,\tau) = \langle (X_1^2(0)X_2^2(0))(X_1^2(\tau)X_2^2(\tau))\rangle$, which can be expanded as

$$C_{\mathcal{E}}(\tau) = \langle X_1^2(0)X_1^2(\tau)\rangle + \langle X_2^2(0)X_2^2(\tau)\rangle + \langle X_1^2(0)X_2^2(\tau)\rangle + \langle X_2^2(0)X_2^2(\tau)\rangle. \tag{C.10}$$

The first two of equation (C.10) are identical and given by equation (C.9), whereas $\langle X_i^2(0)X_j^2(\tau)\rangle_{i\neq j} = \langle X_i^2(0)\rangle \times \langle X_j^2(\tau)\rangle = \langle X_2\rangle^2$, due to the uncorrelated nature of X_1 and X_2 and to the isotropic distribution of the driving fluctuations. Finally, we obtain:

$$\begin{aligned} C_{\mathcal{E}}(\tau) &= 2(C_{X^2}(\tau) + \langle X^2\rangle^2) \\ &= 4\left(\frac{k_BT}{m_{\text{eff}}\omega_0}\right)^2\left(1+e^{-\gamma_{\text{m}}|\tau|}\right), \end{aligned} \tag{C.11}$$

where we have assumed the driving bath to be of a thermal nature with temperature T, $S_F^{th} = 2m_{\text{eff}}\gamma_{\text{m}}k_BT$, yielding to $\langle X^2\rangle = k_BT/m_{\text{eff}}\omega_{\text{m}}^2$. Equation (C.11) shows that the energy autocorrelation function is an exponentially decaying function of time, with a time constant $1/\gamma_{\text{m}}$.

C.2 Two-modes energy autocorrelation

For suspended nanomechanical cantilevers (chapter 6), the mechanical mode of interest comes along with a second mechanical mode associated with the perpendicular direction of vibration. In the frame rotating at the mechanical resonance frequency ω_1 associated with mode 1, the quadratures of the mechanical signal I and Q can be therefore expressed as

$$I(t) = \frac{1}{2}(X_{11}(t) + X_{21}(t)\cos\Delta\omega(t)) + \frac{1}{2}X_{22}(t)\sin\Delta\omega(t) \tag{C.12}$$

$$Q(t) = -\sin X_{21}(t)\sin\Delta\omega t + \frac{1}{2}(X_{12}(t) + X_{22}(t)\cos\Delta\omega t), \tag{C.13}$$

where X_{ij} denote the j^{th} quadrature associated with mode i and with $\Delta\omega = \omega_2 - \omega_1$ the frequency splitting between the two mechanical modes. The "energy" as obtained from I and Q, $\tilde{\mathcal{E}}(t) = I^2(t) + Q^2(t)$ is given by

$$\begin{aligned} \tilde{\mathcal{E}}(t) = \mathcal{E}_1(t) + \mathcal{E}_2(t) &+ 2(X_{11}(t)X_{21}(t) + X_{12}(t)X_{22}(t))\cos\Delta\omega t \\ &+ 2(X_{11}(t)X_{22}(t) - X_{21}(t)X_{12}(t))\sin\Delta\omega t, \end{aligned} \tag{C.14}$$

where we noted $\tilde{\mathcal{E}}_i(t) = X_{i1}^2(t) + X_{i2}^2(t)$ the enrgy of mode i. The autocorrelation $C_{\tilde{\mathcal{E}}}(\tau) = \langle\tilde{\mathcal{E}}(t)\tilde{\mathcal{E}}(t)\rangle$ therefore reads:

$$\begin{aligned} \langle\tilde{\mathcal{E}}(t)\tilde{\mathcal{E}}(0)\rangle = \; & C_{E_1}(\tau) + C_{E_2}(\tau) + \\ & 2\langle(X_{11}(0)X_{21}(0) + X_{12}(0)_{22}(0))(X_{11}(\tau)X_{21}(\tau) + X_{12}(\tau)_{22}(\tau))\cos\Delta\omega\tau\rangle \\ & = C_{\mathcal{E}_1}(t) + C_{\mathcal{E}_2}(t) + 4(C_{11}(\tau)C_{12}(\tau) + C_{12}(\tau)C_{22}(\tau))\cos\Delta\omega\tau, \end{aligned} \tag{C.15}$$

with $C_{ij}(\tau) = \langle X_{ij}(0)X_{ij}(\tau)\rangle$. To obtain equation (C.15), we have utilized the stationarity of the problem $\langle \mathcal{E}(t)\mathcal{E}(t+\tau)\rangle = \langle \mathcal{E}(0)\mathcal{E}(\tau)\rangle$, and we have assumed modes 1 and 2 to be perfectly uncorrelated, $\langle X_{ij}(0)X_{kl}(\tau)\rangle = \delta_{ik}\delta_{jl}C_{ij}(\tau)$ (δ the Kronecker delta symbol). Thereby, equation (C.15) shows that the two-modes energy autocorrelation function writes as the sum of the individual energy autocorrelation functions, plus a beat signal at the splitting frequency $\Delta\omega$. Note that even for negligible splitting ($\Delta\omega \ll \gamma_1,\ \gamma_2$), separating the contributions of each mode remains possible as long as they have distinct mechanical decay rates, which is often the case. Indeed, the sum of the two first terms in Eq. 20 is no longer a purely exponentially decaying function of time, and the deviations from this model therefore enable to accurately address the presence of 2 modes and their corresponding quality factors through the slope irregularities. Note that this would not be equivalent to possible Lorentzian irregularities in the motion spectrum, which is subjected to frequency noise (see below) and does not enable damping extraction to the same level of accuracy.

C.3 Energy autocorrelation in the presence of frequency noise

A widely known advantage of extracting the dissipation properties from the autocorrelation function of the energy is that it is immune to unavoidable sources of frequency noise [150], which becomes critical in the ultra-high Q-factor regime [139, 17].

The energy of a mechanical mode demodulated in a referential rotating frame of $\omega_{\mathrm{d}} \neq \omega_0$, using equation (B.14) is given by

$$\begin{aligned}
\mathcal{E}(\omega_d, t) &= I^2(t) + Q^2(t) \\
&= \frac{1}{4}X_1^2(t)\cos^2(\omega_0-\omega_{\mathrm{d}})t + \frac{1}{4}X_2^2(t)\sin^2(\omega_0-\omega_{\mathrm{d}})t \\
&+ \frac{1}{2}X_1(t)X_2(t)\cos(\omega_0-\omega_{\mathrm{d}})t\ \ \sin(\omega_0-\omega_{\mathrm{d}})t \\
&+ \frac{1}{4}X_1^2(t)\sin^2(\omega_0-\omega_{\mathrm{d}})t + \frac{1}{4}X_2^2(t)\cos^2(\omega_0-\omega_{\mathrm{d}})t \\
&- \frac{1}{2}X_1(t)X_2(t)\cos(\omega_0-\omega_{\mathrm{d}})t\ \ \sin(\omega_0-\omega_{\mathrm{d}})t \\
&= \frac{1}{4}\big[X_1^2(t) + X_2^2(t)\big]. \qquad \text{(C.16)}
\end{aligned}$$

Equation (C.16) therefore shows that the energy does not depend of the demodulation procedure. In particular, this result holds even in presence of frequency noise, that is for $\omega_0 = \omega_{\mathrm{d}} + \delta\omega(t)$, with $\delta\omega(t)$ a slowly varying frequency noise term.

Appendix D

Graphene transfer technique

In this section we are going to present our PMMA supported transfer technique of two-dimensional materials, which was firstly developed at Columbia university [196]. We established this technique as a part of this Ph.D thesis and we further developed and optimized it according to the needs of our experiments. Such a fabrication process is beneficial when there is a need to transfer graphene (or other two-dimensional materials) on top of other structures that are already fabricated. For instance in our work where we coupled a graphene resonator to a superconducting cavity [68] or in graphene resonators where we wanted to implement localized gates to reduce the parasitic capacitances (Figure D.2(b)).

In Figure D.1 the process flow of the PMMA supported transfer technique is briefly illustrated. The process starts by preparing a polymer stack on top of silicon substrates, on which the graphene will be exfoliated. The polymer stack consist of water-soluble layer (PVA) and PMMA 950 (Figure D.1(a)). The PMMA thickness is precisely tuned in order to provide enough contrast for the identification of graphene with optical means. Single and few-layer graphene flakes are selected with an optical microscope by measuring the intensity of the reflected light, similarly as in graphene on top of SiO_2 that is described in section 5.2. The contrast depends on the amount of graphene layers and the thickness of the polymer stack. The intensity per single layer of graphene for each substrate is calibrated after characterizing single and few graphene layers with Raman spectroscopy. After the identification of the graphene flake that will be used for the transfer, the Si-PVA-PMMA chips are placed on the surface of a water bath (Figure D.1(b)). Few minutes afterwards, the PVA is dissolved by water and as a result the Si substrate sinks at the bottom of the water bath while the PMMA-Graphene layer floats on the water surface. A volcano-shaped holder is then used in order to "fish"the membrane from the surface of the water bath (Figure D.1(c)). It is then placed on a heater at 100 C° for 5 min to evaporate the water. Afterwards, the holder is place on a XYZ micro-manipulator mounted on a microscope setup. It is then placed between the objective and the target chip as illustrated in Figure D.1(d). The target substrate lies on a XY motorized stage on top of a heater which is used to evaporate any water that is absorbed on the surface of the target substrate. The microscope objective is used to focus either on the substrate or on the PVA focal plane. The motorized stage and the micro-manipulator provide all the necessary degrees of freedom to align the graphene with respect to the target structure. When everything is aligned, we use the Z-directin of the position to place the

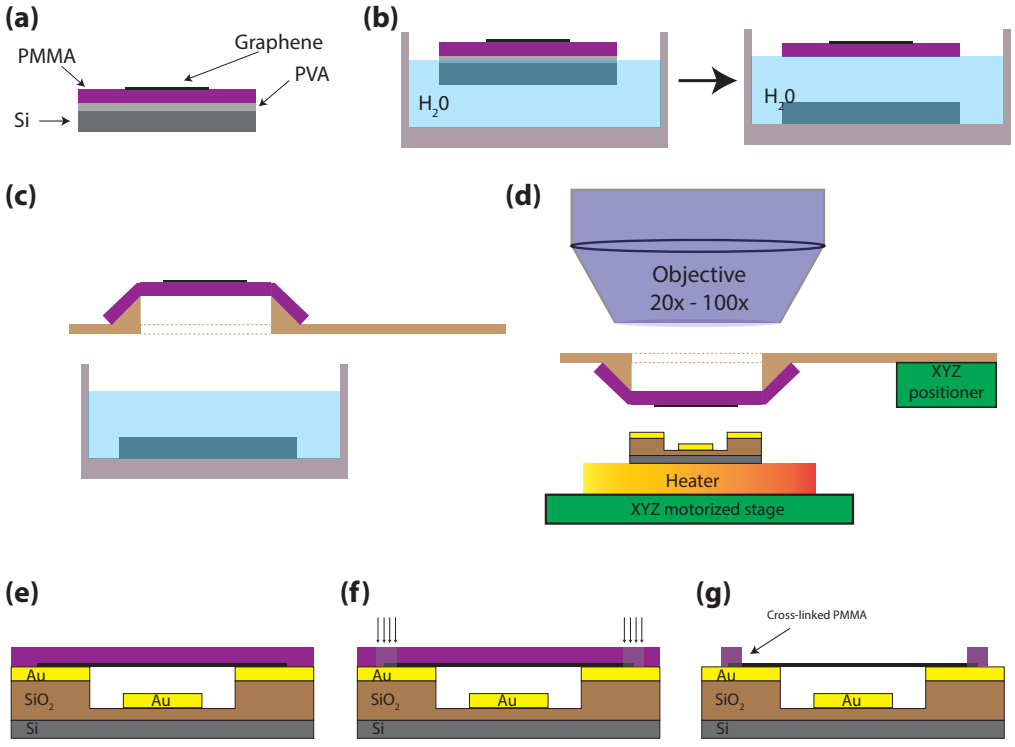

Figure D.1: Graphene PMMA supported transfer technique steps. **(a)** Graphene exfoliation on PVA/PMMA polymer stack. **(b)** PVA dissolution in water results in the release of the PMMA membrane. **(c)** PMMA membrane "fishing"using the volcano-shaped transfer holder. **(d)** Transfer of the PMMA/graphene mebrane on the target substrate. The volcano-shaped holder is attached on a XYZ micro-positioner and the target substrate lies on a XYZ motorized stage. The microscope objective is used to observe both the focal plane of graphene and the one of the target substrate, while the micro-positioner and the motorized stage are used for alignment. **(e)** Transfered membrane on top of the target substrate. **(f)** PMMA cross-linking using electron beam lithography. **(g)** The graphene membrane is released in acetone bath followed by a critical point drying step.

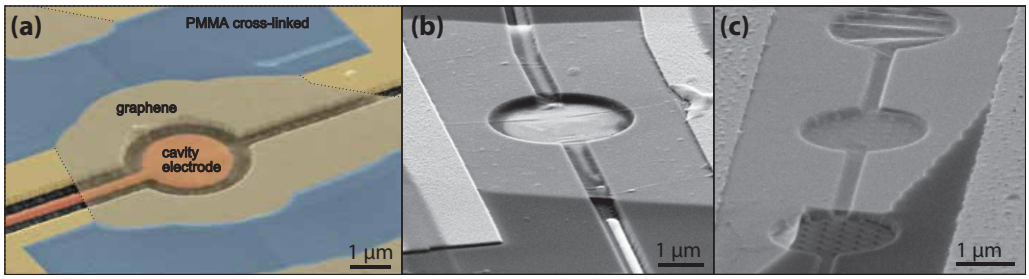

Figure D.2: Examples of graphene resonators that the transfer technique was employed for their fabrication. **(a)** Graphene resonators coupled to a superconducting cavity [68]. **(b)** Graphene resonator in a 3-terminal configuration with a local-gate, fabricated on highly resistive Si substrate to reduce the parasitic capacitances. **(c)** Graphene membranes suspended on top of gold nanoparticle arrays in a distance below 50 nm.

PMMA/graphene membrane on the target substrate (Figure D.1(e)).

A key requirement for most of the nanoresonators that we realized for our experiments is that the separation distance between the graphene and the structure underneath is minimal. For this reason we introduce a development with respect to the original transfer technique: We perform an electron beam lithography step where we cross-link part of the PMMA using a 10000 μC/cm^2 electron beam dose Figure D.1(e). An acetone bath followed by a critical point drying step is used in order to dissolve PMMA and suspend graphene avoiding capillary force, respectively. The cross-linked part of the PMMA is immune to acetone and as a result it remains on the substrate forming supporting clamping pads for the grpahene. This technique allowed to suspend graphene resonators with a separation distance between the counter structure that as low as 50 nm for few micrometer long graphene resonators. In Figure D.2 scanning electron microscope images of graphene mechanical resonators that we fabricated with this technique are illustrated.

Bibliography

[1] R. Hooke. *A description of helioscopes, and some other instruments*. London, 1676.

[2] R. Hooke. *Lecture de potentia restitutiva, or of spring, explaining the power of springing bodies to which are added some collections*. London, 1678.

[3] M. S. Hanay, S. Kelber, A. K. Naik, D. Chi, S. Hentz, E. C. Bullard, E. Colinet, L. Duraffourg, and M. L. Roukes. Single-protein nanomechanical mass spectrometry in real time. *Nature nanotechnology*, 7(9):602–8, sep 2012.

[4] A. N. Cleland and M. L. Roukes. A nanometre-scale mechanical electrometer. *Nature*, 392(6672):160–162, 1998.

[5] H. Okamoto, N. Kitajima, K. Onomitsu, R. Kometani, S. I. Warisawa, S. Ishihara, and H. Yamaguchi. High-sensitivity charge detection using antisymmetric vibration in coupled micromechanical oscillators. *Applied Physics Letters*, 98(1):13–16, 2011.

[6] D. Rugar, R. Budakian, H. J. Mamin, and B. W. Chui. Single spin detection by magnetic resonance force microscopy. *Nature*, 430(6997):329–32, jul 2004.

[7] A. D. O'Connell, M. Hofheinz, M. Ansmann, R. C. Bialczak, M. Lenander, E. Lucero, M. Neeley, D. Sank, H. Wang, M. Weides, J. Wenner, J. M. Martinis, and A. N. Cleland. Quantum ground state and single-phonon control of a mechanical resonator. *Nature*, 464(7289):697–703, apr 2010.

[8] J. D. Teufel, T. Donner, D. Li, J. W. Harlow, M. S. Allman, K. Cicak, A. J. Sirois, J . D. Whittaker, K. W. Lehnert, and R. W. Simmonds. Sideband cooling of micromechanical motion to the quantum ground state. *Nature*, 475(7356):359–363, jul 2011.

[9] J. Chan, T. P. M. Alegre, A. H. Safavi-Naeini, J. T. Hill, A. Krause, S. Groeblacher, M. Aspelmeyer, and O. Painter. Laser cooling of a nanomechanical oscillator into its quantum ground state. *Nature*, 478(7367):18, oct 2011.

[10] T. P. Purdy, R. W. Peterson, and C. A. Regal. Observation of radiation pressure shot noise on a macroscopic object. *Science New York NY*, 339(6121):801–4, feb 2013.

[11] T. A. Palomaki, J. D. Teufel, R. W. Simmonds, and K. W. Lehnert. Entangling mechanical motion with microwave fields. *Science (New York, N.Y.)*, 342(6159):710–3, nov 2013.

[12] S. Shim, M. Imboden, and P. Mohanty. Synchronized oscillation in coupled nanomechanical oscillators. *Science (New York, N.Y.)*, 316(5821):95–99, apr 2007.

[13] A. Eichler, J. Moser, J. Chaste, M. Zdrojek, I. Wilson-Rae, and A. Bachtold. Nonlinear damping in mechanical resonators made from carbon nanotubes and graphene. *Nature nanotechnology*, 6(6):339–342, jun 2011.

[14] J. Chaste, M. Sledzinska, M. Zdrojek, J. Moser, and a. Bachtold. High-frequency nanotube mechanical resonators. *Applied Physics Letters*, 99(21):2011–2014, 2011.

[15] E. A. Laird, F. Pei, W. Tang, G. A. Steele, and L. P. Kouwenhoven. A high quality factor carbon nanotube mechanical resonator at 39 GHz. *Nano Letters*, 12(1):193–197, 2012.

[16] A. K. Hüttel, G. A. Steele, B. Witkamp, M. Poot, L. P. Kouwenhoven, and H. S. J. Van Der Zant. Carbon nanotubes as ultrahigh quality factor mechanical resonators. *Nano Letters*, 9(7):2547–2552, 2009.

[17] J. Moser, A. Eichler, J. Güttinger, M. I. Dykman, and A. Bachtold. Nanotube mechanical resonators with quality factors of up to 5 million. *Nature Nanotechnology*, 9(12):1007–1011, oct 2014.

[18] V. Sazonova, Y. Yaish, H. Ustünel, D. Roundy, T. A. Arias, and P. L. McEuen. A tunable carbon nanotube electromechanical oscillator. *Nature*, 431(7006):284–287, 2004.

[19] C. Chen, S. Rosenblatt, K. I. Bolotin, W. Kalb, P. Kim, I. Kymissis, H. L. Stormer, T. F Heinz, and J. Hone. Performance of monolayer graphene nanomechanical resonators with electrical readout. *Nature nanotechnology*, 4(12):861–867, dec 2009.

[20] J. Chaste, a. Eichler, J. Moser, G. Ceballos, R. Rurali, and a. Bachtold. A nanomechanical mass sensor with yoctogram resolution. *Nature Nanotechnology*, 7(5):301–304, may 2012.

[21] H. Chiu, P. Hung, H. W. C. Postma, and M. Bockrath. Single-atom mass sensing using carbon nanotube resonators. *Preprint*, pages 1–11, 2008.

[22] J. S. Bunch, A. M. van der Zande, S. S. Verbridge, I. W. Frank, D. M. Tanenbaum, J. M. Parpia, H. G. Craighead, and P. L. McEuen. Electromechanical resonators from graphene sheets. *Science (New York, N.Y.)*, 315(5811):490–3, jan 2007.

[23] J. Moser, J. Güttinger, A. Eichler, M. J. Esplandiu, D. E. Liu, M. I. Dykman, and A. Bachtold. Ultrasensitive force detection with a nanotube mechanical resonator. *Nature nanotechnology*, 8(7):493–6, jul 2013.

[24] B. Lassagne, Y. Tarakanov, J. Kinaret, D. Garcia-Sanchez, and A. Bachtold. Coupling mechanics to charge transport in carbon nanotube mechanical resonators. *Science (New York, N.Y.)*, 325(5944):1107–1110, 2009.

[25] G. A. Steele, A. K. Hüttel, B. Witkamp, M. Poot, H. B. Meerwaldt, L. P. Kouwenhoven, and H. S. J. van der Zant. Strong coupling between single-electron tunneling and nanomechanical motion. *Science (New York, N.Y.)*, 325(5944):1103–7, aug 2009.

[26] M. Ganzhorn and W. Wernsdorfer. Dynamics and Dissipation Induced by Single-Electron Tunneling in Carbon Nanotube Nanoelectromechanical Systems. *Physical Review Letters*, 108(17):175502, 2012.

[27] V. Singh, B. Irfan, G. Subramanian, H. S. Solanki, S. Sengupta, S. Dubey, A. Kumar, S. Ramakrishnan, and M. M. Deshmukh. Coupling between quantum Hall state and electromechanics in suspended graphene resonator. *Applied Physics Letters*, 100(23), 2012.

[28] C. Chen. Graphene NanoElectroMechanical Resonators and Oscillators. *Thesis*, 2013.

[29] A. Eichler, M. Del Álamo Ruiz, J. A. Plaza, and A. Bachtold. Strong coupling between mechanical modes in a nanotube resonator. *Physical Review Letters*, 109(2):1–5, jul 2012.

[30] X. Song, M. Oksanen, M. A. Sillanpää, H. G. Craighead, J. M. Parpia, and P. J. Hakonen. Stamp transferred suspended graphene mechanical resonators for radio frequency electrical readout. *Nano letters*, 12(1):198–202, jan 2012.

[31] K. S. Novoselov, A. K. Geim, S. V. Morozov, D. Jiang, Y. Zhang, S. V. Dubonos, I. V. Grigorieva, and A . A. Firsov. Electric Field Effect in Atomically Thin Carbon Films. *Science*, 306(5696):666–669, oct 2004.

[32] A. K. Geim and K. S. Novoselov. The rise of graphene. *Nat. Mater.*, 6(3):183–191, 2007.

[33] S. Stankovich, D. A. Dikin, G. H. B. Dommett, K. M. Kohlhaas, E. J. Zimney, E. A. Stach, R. D. Piner, S. T. Nguyen, and R. S. Ruoff. Graphene-based composite materials. *Nature*, 442(7100):282–286, 2006.

[34] J. C. Meyer, A. K. Geim, M. I. Katsnelson, K. S. Novoselov, T. J. Booth, and S. Roth. The structure of suspended graphene sheets. *Nature*, 446(7131):60–63, 2007.

[35] S. Iijima. Helical microtubules of graphitic carbon. *Nature*, 354(6348):56–58, 1991.

[36] P. R. Wallace. The band theory of graphite. *Physical Review*, 71(9):622–634, 1947.

[37] A. H. Castro Neto, F. Guinea, N. M. R. Peres, K. S. Novoselov, and A. K. Geim. The electronic properties of graphene. *Reviews of Modern Physics*, 81(1):109–162, 2009.

[38] K.I. Bolotin, K.J. Sikes, Z. Jiang, M. Klima, G. Fudenberg, J. Hone, P. Kim, and H.L. Stormer. Ultrahigh electron mobility in suspended graphene. *Solid State Communications*, 146(9-10):351–355, 2008.

[39] X. Du, I. Skachko, A. Barker, and E. Y. Andrei. Approaching ballistic transport in suspended graphene. *Nature Nanotechnology*, 3(8):491–495, 2008.

[40] D. C. Elias, R. V. Gorbachev, A. S. Mayorov, S. V. Morozov, A. A. Zhukov, P. Blake, L. A. Ponomarenko, I. V. Grigorieva, K. S. Novoselov, F. Guinea, and A. K. Geim. Dirac cones reshaped by interaction effects in suspended graphene. *Nature Physics*, 7(9):701–704, 2011.

[41] I. Meric, M. Y. Han, A. F. Young, B. Ozyilmaz, P. Kim, and K. L. Shepard. Current saturation in zero-bandgap, top-gated graphene field-effect transistors. *Nature nanotechnology*, 3(11):654–659, 2008.

[42] R. Saito, M. S. Dresselhaus, and G. Dresselhaus. *Physical Properties of Carbon Nanotubes*. Imperial College Press, 1998.

[43] M. S. Dresselhaus, G. Dresselhaus, and P. A. Vouris. *Carbon Nanotubes: Synthesis, Structure, Properties, and Applications*, volume 27. Springer, 2001.

[44] T. Dürkop, S. A. Getty, E. Cobas, and M. S. Fuhrer. Extraordinary Mobility in Semiconducting Carbon Nanotubes. *Nano Letters*, 4(1):35–39, 2004.

[45] A. Vargas Lugo Cantu. *No Optical Properties of Electrostatically Charged Carbon Nanotubes*. PhD thesis, ETH Zurich, 2014.

[46] T. Ando, Y. Zheng, and H. Suzuura. Dynamical Conductivity and Zero-Mode Anomaly in Honeycomb Lattices. *Journal of the Physical Society of Japan*, 71(5):1318–1324, 2002.

[47] R. R. Nair, P. Blake, A. N. Grigorenko, K. S. Novoselov, T. J. Booth, T. Stauber, N. M. R. Peres, and A. K. Geim. Fine structure constant defines visual transparency of graphene. *Science (New York, N.Y.)*, 320(5881):1308, jun 2008.

[48] A. B. Kuzmenko, E. van Heumen, F. Carbone, and D. van der Marel. Universal Optical Conductance of Graphite. *Physical Review Letters*, 100(11):117401, 2008.

[49] G. R. A. Jamal and S. M. Mominuzzaman. Limitations of Tight Binding Model in Describing Electronic Properties of Single Wall Carbon Nanotubes. *Journal of Nanoscience and Nanoengineering*, 1(2):96–106, 2015.

[50] Q. Zhao, M. Nardelli, and J. Bernholc. Ultimate strength of carbon nanotubes: A theoretical study. *Physical Review B*, 65(14):1–6, 2002.

[51] O. L. Blakslee. Elastic Constants of Compression-Annealed Pyrolytic Graphite. *Journal of Applied Physics*, 41(8):3373, 1970.

[52] B. T. Kelly. *Physics of graphite*, volume 114. Applied Science London, 1983.

[53] E. W. Wong, P. E. Sheehan, and C. M. Lieber. Nanobeam mechanics: elasticity, strength, and toughness of nanorods and nanotubes. *Science*, 277(5334):1971–1975, 1997.

[54] E. D. Minot, Y. Yaish, V. Sazonova, Ji-Yong Park, M. Brink, and P. L. McEuen. Tuning carbon nanotube band gaps with strain. *Physical review letters*, 90(15):156401, 2003.

[55] C. Lee, X. Wei, J. W. Kysar, and J. Hone. Measurement of the Elastic Properties and Intrinsic Strength of Monolayer Graphene. *Science*, 321(July):385–388, 2008.

[56] Min-Feng Yu, Bradley Files, Sivaram Arepalli, and Rodney Ruoff. Tensile Loading of Ropes of Single Wall Carbon Nanotubes and their Mechanical Properties. *Physical Review Letters*, 84(24):5552–5555, 2000.

[57] C. Y. Wang, K. Mylvaganam, and L. C. Zhang. Wrinkling of monolayer graphene: A study by molecular dynamics and continuum plate theory. *Physical Review B - Condensed Matter and Materials Physics*, 80(15):1–5, 2009.

[58] L. D. Landau and E. M. Lifshitz. *Theory of elasticity*, volume 7. 1965.

[59] M. Poot and H. S. J. van der Zant. Mechanical systems in the quantum regime. *Physics Reports*, 511(5):273–335, 2012.

[60] R. B. Karabalin, M. C. Cross, and M. L. Roukes. Nonlinear dynamics and chaos in two coupled nanomechanical resonators. *Physical Review B*, 79(16):165309, apr 2009.

[61] H .J. R. Westra, M. Poot, H. S. J. van der Zant, and W. J. Venstra. Nonlinear modal interactions in clamped-clamped mechanical resonators. *Physical review letters*, 105(11):117205, sep 2010.

[62] C. Chatfield. *The analysis of time series : an introduction*. 2004.

[63] H. B. Callen and T. A. Welton. Irreversibility and Generalized Noise. *Physical Review*, 83(1):34–40, 1951.

[64] L. D. Landau, E. M. Lifshitz, and R. L. E. *Statistical Physics, Part 1*, volume 34. 1981.

[65] H. Nyquist. Thermal Agitation of Electric Charge in Conductors. *Phys. Rev.*, 32(1):110–113, jul 1928.

[66] K. L. Ekinci and M. L. Roukes. Nanoelectromechanical systems. *Review of Scientific Instruments*, 76(6):061101, 2005.

[67] R. Lifshitz and M. C. Cross. Nonlinear Dynamics of Nanomechanical and Micromechanical Resonators. *Reviews of Nonlinear Dynamics and Complexity*, pages 1–52, 2009.

[68] P. Weber, J. Güttinger, I. Tsioutsios, D. E. Chang, and a. Bachtold. Coupling graphene mechanical resonators to superconducting microwave cavities. *Nano Letters*, 14(5):2854–2860, apr 2014.

[69] B. Ilic, S. Krylov, K. Aubin, R. Reichenbach, and H. G. Craighead. Optical excitation of nanoelectromechanical oscillators. *Applied Physics Letters*, 86(19):1–3, 2005.

[70] A. N. Cleland and M. L. Roukes. Fabrication of high frequency nanometer scale mechanical resonators from bulk Si crystals. *Applied Physics Letters*, 69(18):2653–2655, 1996.

[71] K. L. Ekinci, Y. T. Yang, X. M H Huang, and M. L. Roukes. Balanced electronic detection of displacement in nanoelectromechanical systems. *Applied Physics Letters*, 81(12):2253–2255, 2002.

[72] S. C. Masmanidis, R. B. Karabalin, I. De Vlaminck, G. Borghs, M. R. Freeman, and M. L. Roukes. Multifunctional nanomechanical systems via tunably coupled piezoelectric actuation. *Science (New York, N.Y.)*, 317(5839):780–783, aug 2007.

[73] I. Bargatin, E. B. Myers, J. Arlett, B. Gudlewski, and M. L. Roukes. Sensitive detection of nanomechanical motion using piezoresistive signal downmixing. *Applied Physics Letters*, 86(13):1–3, 2005.

[74] W. C. Tang, Tu-Cuong H. Nguyen, M. W. Judy, and R. T. Howe. Electrostatic-comb drive of lateral polysilicon resonators. *Sensors and Actuators A: Physical*, 21:328–331, 1990.

[75] Clark T.-C. Nguyen. MEMS technology for timing and frequency control. *IEEE transactions on ultrasonics, ferroelectrics, and frequency control*, 54(2):251–70, mar 2007.

[76] R. G. Knobel and A. N Cleland. Nanoscale Displacement Sensing using a Single Electron Transistor. *Measurement*, 424(July):291–293, 2003.

[77] V. Gouttenoire, T. Barois, S. Perisanu, J. L. Leclercq, S. T. Purcell, P. Vincent, and A. Ayari. Digital and FM demodulation of a doubly clamped single-walled carbon-nanotube oscillator: Towards a nanotube cell phone. *Small*, 6(9):1060–1065, may 2010.

[78] A. M. van der Zande, R. A. Barton, J. S Alden, C. S. Ruiz-Vargas, W. S. Whitney, P. H. Q. Pham, J. Park, J. M. Parpia, H. G Craighead, and P. L. McEuen. Large-Scale Arrays of Single-Layer Graphene Resonators. *Nano letters*, pages 4869–4873, nov 2010.

[79] B. H. Schneider, V. Singh, W. J. Venstra, H. B. Meerwaldt, and G. A. Steele. Observation of decoherence in a carbon nanotube mechanical resonator. *Nature communications*, 5:5819, 2014.

[80] Y. Xu, C. Chen, V. V. Deshpande, F. A. DiRenno, A. Gondarenko, D. B. Heinz, S. Liu, P. Kim, and J. Hone. Radio frequency electrical transduction of graphene mechanical resonators. *Applied Physics Letters*, 97(24):243111, 2010.

[81] M. Aspelmeyer, T. J. Kippenberg, and F. Marquard. Cavity optomechanics. *Reviews of Modern Physics*, 86(4):1391–1452, 2014.

[82] X. Song, M. Oksanen, J. Li, P. J. Hakonen, and M. A. Sillanpää. Graphene Optomechanics Realized at Microwave Frequencies. *Physical Review Letters*, 113(2):027404, jul 2014.

[83] V. Singh, S. J. Bosman, B. H. Schneider, Y. M. Blanter, A. Castellanos-Gomez, and G. A. Steele. Optomechanical coupling between a multilayer graphene mechanical resonator and a superconducting microwave cavity. *Nature nanotechnology*, 9(10):820–4, 2014.

[84] S. Akita, S. Sawaya, and Y. Nakayama. Energy loss of carbon nanotube cantilevers for mechanical vibration. *Japanese Journal of Applied Physics Part 1-Regular Papers Brief Communications & Review Papers*, 46(9B):6295–6298, 2007.

[85] S. Sawano, T. Arie, and S. Akita. Carbon nanotube resonator in liquid. *Nano Letters*, 10(9):3395–3398, 2010.

[86] S. Stapfner, L. Ost, D. Hunger, J. Reichel, I. Favero, and E. M. Weig. Cavity-enhanced optical detection of carbon nanotube Brownian motion. *Applied Physics Letters*, 102, 2013.

[87] J. T. Robinson, M. Zalalutdinov, Jeffrey W. Baldwin, E. S. Snow, Z. Wei, P. Sheehan, and B. H. Houston. Wafer-scale reduced graphene oxide films for nanomechanical devices. *Nano Letters*, 8(10):3441–3445, 2008.

[88] S. Shivaraman, R. A. Barton, X Yu, J. Alden, L. Herman, M. S. V. Chandrashekhar, J. Park, P. L. McEuen, J. M. Parpia, H. G. Craighead, and M. G. Spencer. Free-standing epitaxial graphene. *Nano Letters*, 9(9):3100–3105, 2009.

[89] Robert a. Barton, B. Ilic, Arend M. Van Der Zande, William S. Whitney, Paul L. McEuen, Jeevak M. Parpia, and Harold G. Craighead. High, size-dependent quality factor in an array of graphene mechanical resonators. *Nano Letters*, 11(3):1232–1236, 2011.

[90] R. A. Barton, I. R. Storch, V. P. Adiga, R. Sakakibara, B. R. Cipriany, B. Ilic, S. P. Wang, P. Ong, P. L. McEuen, J. M. Parpia, and H. G. Craighead. Photothermal self-oscillation and laser cooling of graphene optomechanical systems. *Nano letters*, 12(9):4681–6, 2012.

[91] D. Garcia-Sanchez, a. San Paulo, M. J. Esplandiu, F. Perez-Murano, L. Forró, a. Aguasca, and a. Bachtold. Mechanical detection of carbon nanotube resonator vibrations. *Physical Review Letters*, 99(8):1–4, aug 2007.

[92] A. M. van der Zande, A. S. Paulo, B Lassagne, P. L. Mceuen, and A. Bachtold. Imaging Mechanical Vibrations in Suspended Graphene Sheets 2008. *Nano letters*, 2008.

[93] M. M. J. Treacy, T. W. Ebbesen, and J. M. Gibson. Exceptionally high Young's modulus observed for individual carbon nanotubes, 1996.

[94] B. Babić, J. Furer, S. Sahoo, S. Farhangfar, and C. Schönenberger. Intrinsic Thermal Vibrations of Suspended Doubly Clamped Single-Wall Carbon Nanotubes. *Nano Letters*, 3(11):1577–1580, 2003.

[95] I. Tsioutsios, J. Moser, J. A. Plaza, and A. Bachtold. Controlled assembly of graphene sheets and nanotubes: Fabrication of suspended multi-element all-carbon vibrational structures. *Journal of Applied Physics*, 114(10):104310, 2013.

[96] J. G. Yoder. Christiaan huygens, book on the pendulum clock (1673). *Landmark Writings in Western Mathematics 1640-1940*, (1673):33–45, 2005.

[97] M. Sato, B. E. Hubbard, L. Q. English, A. J. Sievers, B. Ilic, D. A. Czaplewski, and H. G. Craighead. Study of intrinsic localized vibrational modes in micromechanical oscillator arrays. *Chaos*, 13(January):702–715, jan 2003.

[98] M. C. Cross, A. Zumdieck, R. Lifshitz, and J. L. Rogers. Synchronization by nonlinear frequency pulling. *Physical Review Letters*, 93(November):1–4, nov 2004.

[99] H. Okamoto, A. Gourgout, C. Chang, K. Onomitsu, I. Mahboob, E. Y. Chang, and H. Yamaguchi. Coherent phonon manipulation in coupled mechanical resonators. *Nature Physics*, 9(8):480–484, jul 2013.

[100] T. Rocheleau, T. Ndukum, C. Macklin, J. B. Hertzberg, A. A. Clerk, and K. C. Schwab. Preparation and detection of a mechanical resonator near the ground state of motion. *Nature*, 463(7277):72–75, jan 2010.

[101] E. Verhagen, S. Deléglise, S. Weis, A. Schliesser, and T. J. Kippenberg. Quantum-coherent coupling of a mechanical oscillator to an optical cavity mode. *Nature*, 482(7383):63–67, 2012.

[102] D. H. Santamore, A. C. Doherty, and M. C. Cross. Quantum nondemolition measurement of Fock states of mesoscopic mechanical oscillators. *Physical Review B*, 70(14):144301, oct 2004.

[103] Y. W. Lin, L. W. Hung, S. S. Li, Z. Ren, and Clark T.-C. Nguyen. Quality factor boosting via mechanically-coupled arraying. In *TRANSDUCERS and EUROSENSORS '07 - 4th International Conference on Solid-State Sensors, Actuators and Microsystems*, pages 2453–2456, 2007.

[104] F. D. Bannon, S. Member, J. R. Clark, and C. T. Nguyen. High- Q HF Microelectromechanical Filters. *Science*, 1(4):512–526, 2000.

[105] M. Spletzer, A. Raman, A. Q. Wu, X. Xu, and R. Reifenberger. Ultrasensitive mass sensing using mode localization in coupled microcantilevers. *Applied Physics Letters*, 88(25), 2006.

[106] M. Spletzer, A. Raman, H. Sumali, and J. P. Sullivan. Highly sensitive mass detection and identification using vibration localization in coupled microcantilever arrays. *Applied Physics Letters*, 92(11):2006–2009, 2008.

[107] E. Gil-Santos, D. Ramos, A. Jana, M. Calleja, A. Raman, and J. Tamayo. Mass sensing based on deterministic and stochastic responses of elastically coupled nanocantilevers. *Nano letters*, 9(12):4122–7, 2009.

[108] R. B. Karabalin, R. Lifshitz, M. C. Cross, M. H. Matheny, S. C. Masmanidis, and M. L. Roukes. Signal Amplification by Sensitive Control of Bifurcation Topology. *Physical Review Letters*, 106(9):094102, feb 2011.

[109] B. Reulet, a. Kasumov, M. Kociak, R. Deblock, I. Khodos, Yu. Gorbatov, V. Volkov, C. Journet, and H. Bouchiat. Acoustoelectric Effects in Carbon Nanotubes. *Physical Review Letters*, 85(13):2829–2832, 2000.

[110] A. Reserbat-Plantey, L. Marty, O. Arcizet, N. Bendiab, and V. Bouchiat. A local optical probe for measuring motion and stress in a nanoelectromechanical system. *Nature Nanotechnology*, 7(3):151–155, 2012.

[111] S. Perisanu, T. Barois, P. Poncharal, T. Gaillard, a. Ayari, S. T. Purcell, and P. Vincent. The mechanical resonances of electrostatically coupled nanocantilevers. *Applied Physics Letters*, 98(2011):2009–2012, 2011.

[112] P. Blake and E. W. Hill. Making graphene visible. *Applied Physics Letters*, 91(6):063124, 2007.

[113] B. Gao, Y. F. Chen, M. S. Fuhrer, D. C. Glattli, and A. Bachtold. Four-Point Resistance of Individual Single-Wall Carbon Nanotubes. *Physical Review Letters*, 95(19):196802, 2005.

[114] B. Gao, D. Glattli, B. Plaçais, and A. Bachtold. Cotunneling and one-dimensional localization in individual disordered single-wall carbon nanotubes: Temperature dependence of the intrinsic resistance. *Physical Review B*, 74(8):1–5, 2006.

[115] V. Singh, S. Sengupta, H. S. Solanki, R. Dhall, A. Allain, S. Dhara, P. Pant, and M. M. Deshmukh. Probing thermal expansion of graphene and modal dispersion at low-temperature using graphene nanoelectromechanical systems resonators. *Nanotechnology*, 21(16):165204, apr 2010.

[116] A. M. Goossens, V. E. Calado, A. Barreiro, K. Watanabe, T. Taniguchi, and L. M. K. Vandersypen. Mechanical cleaning of graphene. *Applied Physics Letters*, 100(7):073110, 2012.

[117] R. Karabalin. *Nonlinear, Parametric, and Coupled Nanoelectromechanical Systems*. PhD thesis, CALIFORNIA INSTITUTE OF TECHNOLOGY, 2008.

[118] A. Castellanos-Gomez, H. B. Meerwaldt, W. J. Venstra, H. S. J. van der Zant, and G. A. Steele. Strong and tunable mode coupling in carbon nanotube resonators. *Physical Review B*, 86(4):041402, jul 2012.

[119] J. Gieseler, M. Spasenovic, L. Novotny, and R. Quidant. Nonlinear mode coupling and synchronization of a vacuum-trapped nanoparticle. *Physical Review Letters*, 112(10):1–5, 2014.

[120] T. Faust, J. Rieger, M. J. Seitner, P. Krenn, J. P. Kotthaus, and E. M. Weig. Nonadiabatic dynamics of two strongly coupled nanomechanical resonator modes. *Physical Review Letters*, 109(3):1–4, jul 2012.

[121] T. Faust, J. Rieger, M. J. Seitner, J. P. Kotthaus, and E. M. Weig. Coherent control of a classical nanomechanical two-level system. *Nature Physics*, 9(8):485–488, 2013.

[122] H. W. Ch. Postma, I. Kozinsky, a. Husain, and M. L. Roukes. Dynamic range of nanotube- and nanowire-based electromechanical systems. *Applied Physics Letters*, 86(22):223105, 2005.

[123] A. Voje, J. M. Kinaret, and A. Isacsson. Generating macroscopic superposition states in nanomechanical graphene resonators. *Physical Review B - Condensed Matter and Materials Physics*, 85(20):1–5, 2012.

[124] H. G. Craighead. Nanoelectromechanical systems. *Science (New York, N.Y.)*, 290(5496):1532–6, 2000.

[125] E. E. Wollman, C. U. Lei, a. J. Weinstein, J. Suh, A. Kronwald, F. Marquardt, a. a. Clerk, and K. C. Schwab. Quantum squeezing of motion in a mechanical resonator. *Science*, 349(October 2014):952–955, 2015.

[126] A. Benyamini, A. Hamo, S. V. Kusminskiy, F. von Oppen, and S. Ilani. Real-space tailoring of the electronâĂŞphonon coupling in ultraclean nanotube mechanical resonators. *Nature Physics*, 9(11):1–6, jan 2014.

[127] E. Gavartin, P. Verlot, and T. J. Kippenberg. A hybrid on-chip optomechanical transducer for ultrasensitive force measurements. *Nature Nanotechnology*, 7(June):509–514, 2012.

[128] S. L. Braunstein and C. M. Caves. Statistical distance and the geometry of quantum states. *Physical Review Letters*, 72(22):3439–3443, 1994.

[129] D. Braun. Ultimate quantum bounds on mass measurements with a nanomechanical resonator. *EPL (Europhysics Letters)*, 94(6):68007, 2011.

[130] M. T. Jaekel and S. Reynaud. Quantum Limits in Interferometric Measurements. *EPL (Europhysics Letters)*, 13(4):301, 1990.

[131] T. R. Albrecht, P. Grütter, D. Horne, and D. Rugar. Frequency modulation detection using high-Q cantilevers for enhanced force microscope sensitivity. *Journal of Applied Physics*, 69(2):668–673, 1991.

[132] A. N. Cleland and M. L. Roukes. Noise processes in nanomechanical resonators. *Journal of Applied Physics*, 92(5):2758–2769, 2002.

[133] M. Dykman. *Fluctuating nonlinear oscillators: from nanomechanics to quantum superconducting circuits*. Oxford University Press, 2012.

[134] A. W. Barnard, V. Sazonova, A. M. van der Zande, and P. L. McEuen. Fluctuation broadening in carbon nanotube resonators. *Proceedings of the National Academy of Sciences of the United States of America*, 109(47):19093–6, 2012.

[135] P. Pine, Y. E. Yaish, and J. Adler. Vibrational analysis of thermal oscillations of single-walled carbon nanotubes under axial strain. *Physical Review B - Condensed Matter and Materials Physics*, 89(11):1–7, 2014.

[136] H. Koh, J. J Cannon, T. Shiga, J. Shiomi, S. Chiashi, and S. Maruyama. Thermally induced nonlinear vibration of single-walled carbon nanotubes. *Physical Review B*, 92(2):024306, 2015.

[137] Y. Zhang and M. I. Dykman. Spectral effects of dispersive mode coupling in driven mesoscopic systems. *Physical Review B - Condensed Matter and Materials Physics*, 92(16):1–15, 2015.

[138] Y. Zhang, J. Moser, J. Guttinger, A. Bachtold, and M. I. Dykman. Interplay of driving and frequency noise in the spectra of vibrational systems. *Physical Review Letters*, 113(25):1–10, 2014.

[139] E. Gavartin, P. Verlot, and T. J. Kippenberg. Stabilization of a linear nanomechanical oscillator to its thermodynamic limit. *Nature communications*, 4:2860, dec 2013.

[140] I. Tittonen, G. Breitenbach, T. Kalkbrenner, T. Müller, R. Conradt, S. Schiller, E. Steinsland, N. Blanc, and N. F. de Rooij. Interferometric measurements of the position of a macroscopic body: Towards observation of quantum limits. *Phys. Rev. A*, 59(2):1038–1044, feb 1999.

[141] T. Briant, P. F. Cohadon, M. Pinard, and A. Heidmann. Optical phase-space reconstruction of mirror motion at the attometer level. *The European Physical Journal D - Atomic, Molecular and Optical Physics*, 22(1):131–140, 2003.

[142] M. C. Wang and G. E. Uhlenbeck. On the Theory of the Brownian Motion II. *Rev. Mod. Phys.*, 17(2-3):323–342, apr 1945.

[143] E. Buks and M. L. Roukes. Stiction, adhesion energy, and the Casimir effect in micromechanical systems. *Phys. Rev. B*, 63(3):33402, jan 2001.

[144] A. Niguès, A. Siria, and P. Verlot. Dynamical Backaction Cooling with Free Electrons. *Nat Commun*, 6(8104):8, sep 2015.

[145] M. Imboden and P. Mohanty. Dissipation in nanoelectromechanical systems. *Physics Reports*, 534(3):89–146, 2014.

[146] A. Krishnan, E. Dujardin, T. Ebbesen, P. Yianilos, and M. Treacy. Young's modulus of single-walled nanotubes. *Physical Review B*, 58(20):14013–14019, nov 1998.

[147] J. M. Nichol, R. Budakian, E. R. Hemesath, and L. J. Lauhon. Displacement detection of silicon nanowires by polarization-enhanced fiber-optic interferometry. *Applied Physics Letters*, 93(19):2006–2009, 2008.

[148] E. Gil-Santos, D. Ramos, J. Martínez, M. Fernández-Regúlez, R. García, A. San Paulo, M. Calleja, and J. Tamayo. Nanomechanical mass sensing and stiffness spectrometry based on two-dimensional vibrations of resonant nanowires. *Nature nanotechnology*, 5(9):641–645, 2010.

[149] A. Gloppe, P. Verlot, E. Dupont-Ferrier, A. Siria, P. Poncharal, G. Bachelier, P. Vincent, O. Arcizet, E. Dupont-Ferrier, A. Siria, P. Poncharal, G. Bachelier, P. Vincent, and O. Arcizet. Bidimensional nano-optomechanics and topological backaction in a non-conservative radiation force field. *Nature nanotechnology*, 9(11):920–926, sep 2014.

[150] B. Stipe, H. Mamin, T. Stowe, T. Kenny, and D. Rugar. Noncontact Friction and Force Fluctuations between Closely Spaced Bodies. *Physical Review Letters*, 87(9):096801, aug 2001.

[151] L. G. Villanueva, R. B. Karabalin, M. H. Matheny, D. Chi, J. E. Sader, and M. L. Roukes. Nonlinearity in nanomechanical cantilevers. *Physical Review B - Condensed Matter and Materials Physics*, 87(2):1–8, 2013.

[152] A. Vinante. Thermal frequency noise in micromechanical resonators due to nonlinear mode coupling. *Physical Review B - Condensed Matter and Materials Physics*, 90(2):1–5, 2014.

[153] D. Rugar and P. Grütter. Mechanical parametric amplification and thermomechanical noise squeezing. *Physical Review Letters*, 67(6):699–702, 1991.

[154] A. Naik, O. Buu, M. D. LaHaye, A. D. Armour, A. A. Clerk, M. P. Blencowe, and K. C. Schwab. Cooling a nanomechanical resonator with quantum back-action. *Nature*, 443(7108):193–6, 2006.

[155] T. Richter and W. Vogel. Nonclassicality of quantum states: a hierarchy of observable conditions. *Physical review letters*, 89(28 Pt 1):283601, 2002.

[156] A. Eichler, J. Moser, M. I. Dykman, and A. Bachtold. Symmetry breaking in a mechanical resonator made from a carbon nanotube. *Nature communications*, 4:2843, 2013.

[157] T. Caniard, P. Verlot, T. Briant, P. F. Cohadon, and A. Heidmann. Observation of back-action noise cancellation in interferometric and weak force measurements. *Physical Review Letters*, 99(11):1–4, 2007.

[158] W. Ding, D. A. Dikin, X. Chen, R. D. Piner, R. S. Ruoff, E. Zussman, X. Wang, and X. Li. Mechanics of hydrogenated amorphous carbon deposits from electron-beam-induced deposition of a paraffin precursor. *Journal of Applied Physics*, 98(1):0–7, 2005.

[159] S. Olcum, N. Cermak, S. C. Wasserman, K. S. Christine, H. Atsumi, K. R. Payer, W. Shen, J. Lee, A. M. Belcher, S. N. Bhatia, and S. R. Manalis. Weighing nanoparticles in solution at the attogram scale. *Proceedings of the National Academy of Sciences of the United States of America*, 111(4):1310–5, 2014.

[160] V. B. Braginsky, F. Y. Khalili, and K. S. Thorne. *Quantum Measurement*. Cambridge University Press, 1995.

[161] I. Wilson-Rae, P. Zoller, and a. Imamoáÿąlu. Laser Cooling of a Nanomechanical Resonator Mode to its Quantum Ground State. *Physical Review Letters*, 92(7):075507, feb 2004.

[162] I. Yeo, P-L. de Assis, A. Gloppe, E. Dupont-Ferrier, P. Verlot, N. S. Malik, E. Dupuy, J. Claudon, J-M. Gérard, A. Auffèves, G. Nogues, S. Seidelin, J-Ph. Poizat, O. Arcizet, and M. Richard. Strain-mediated coupling in a quantum dotâĂŞmechanical oscillator hybrid system. *Nature Nanotechnology*, 9(2):106–110, 2013.

[163] J. Teissier, A. Barfuss, P. Appel, E. Neu, and P. Maletinsky. Strain Coupling of a Nitrogen-Vacancy Center Spin to a Diamond Mechanical Oscillator. *Physical Review Letters*, 113(2):020503, 2014.

[164] M. Montinaro, G. Wüst, M. Munsch, Y. Fontana, E. Russo-Averchi, M. Heiss, A. Fontcuberta I Morral, R. J. Warburton, and M. Poggio. Quantum dot optomechanics in a fully self-assembled nanowire. *Nano Letters*, 14(8):4454–4460, may 2014.

[165] F. Wang, G. Dukovic, L. E. Brus, and T. F. Heinz. The optical resonances in carbon nanotubes arise from excitons. *Science (New York, N.Y.)*, 308(5723):838–41, may 2005.

[166] M. S. Hofmann, J. T. Glückert, J. Noé, C. Bourjau, R. Dehmel, and A. Högele. Bright, long-lived and coherent excitons in carbon nanotube quantum dots. *Nature Nanotechnology*, 8(7):502–505, jul 2013.

[167] Y. Miyauchi, M. Iwamura, S. Mouri, T. Kawazoe, M. Ohtsu, and K. Matsuda. Brightening of excitons in carbon nanotubes on dimensionality modification. *Nature Photonics*, 7(9):715–719, jul 2013.

[168] H. Suzuura and T. Ando. Phonons and electron-phonon scattering in carbon nanotubes. *Physical Review B*, 65(23):235412, may 2002.

[169] E. Mariani and F. von Oppen. Electron-vibron coupling in suspended carbon nanotube quantum dots. *Physical Review B*, 80(15):155411, oct 2009.

[170] I. Wilson-Rae, C. Galland, W. Zwerger, and A. Imamoglu. Exciton-assisted optomechanics with suspended carbon nanotubes. *New Journal of Physics*, 14(11):115003, 2012.

[171] S. M. Bachilo, M. S. Strano, C. Kittrell, R. H. Hauge, R. E. Smalley, and R. B. Weisman. Structure-assigned optical spectra of single-walled carbon nanotubes. *Science*, 298(5602):2361–6, 2002.

[172] A. G. Walsh, A. Nickolas Vamivakas, Y. Yin, S. B. Cronin, M. Selim Ünlü, B. B. Goldberg, and A. K. Swan. Scaling of exciton binding energy with external dielectric function in carbon nanotubes. *Physica E: Low-dimensional Systems and Nanostructures*, 40(7):2375–2379, 2008.

[173] E. Chang, G. Bussi, A. Ruini, and E. Molinari. Excitons in Carbon Nanotubes: An Ab Initio Symmetry-Based Approach. *Physical Review Letters*, 92(19):196401, 2004.

[174] M. A. Semina, R. A. Sergeev, and R. A. Suris. The binding energy of excitons and X + and X âĹŠ trions in one-dimensional systems. *Semiconductors*, 42(12):1427–1433, 2008.

[175] D. A. Tsyboulski, John-David R. Rocha, S. M. Bachilo, L. Cognet, and R. B. Weisman. Structure-dependent fluorescence efficiencies of individual single-walled carbon nanotubes. *Nano letters*, 7(10):3080–5, 2007.

[176] S. Berger, C. Voisin, G. Cassabois, C. Delalande, P. Roussignol, and X. Marie. Temperature dependence of exciton recombination in semiconducting single-wall carbon nanotubes. *Nano letters*, 7(2):398–402, 2007.

[177] I. Sarpkaya, Z. Zhang, W. Walden-Newman, X. Wang, J. Hone, C. W. Wong, and S. Strauf. Prolonged spontaneous emission and dephasing of localized excitons in air-bridged carbon nanotubes. *Nature communications*, 4:2152, jan 2013.

[178] B. K. Ridley. *Quantum Processes in Semiconductors*, volume 1999. OUP Oxford, 1999.

[179] D. J. Heinzen and D. J. Wineland. Quantum-limited cooling and detection of radio-frequency oscillations by laser-cooled ions. *Physical Review A*, 42(5):2977–2994, 1990.

[180] D. Leibfried, R. Blatt, C. Monroe, and D. Wineland. Quantum dynamics of single trapped ions. *Reviews of Modern Physics*, 75(1):281–324, 2003.

[181] P. Treutlein, C. Genes, K. Hammerer, M. Poggio, and P. Rabl. Hybrid Mechanical Systems. *arXiv:1210.4151 [cond-mat, physics:physics, physics:quant-ph]*, pages 327–351, 2014.

[182] V. Perebeinos and P. Avouris. Phonon and Electronic Nonradiative Decay Mechanisms of Excitons in Carbon Nanotubes. *Physical Review Letters*, 101(5):057401, jul 2008.

[183] J. J. Crochet, J. G. Duque, J. H. Werner, and S. K. Doorn. Photoluminescence imaging of electronic-impurity-induced exciton quenching in single-walled carbon nanotubes. *Nature Nanotechnology*, 7(2):126–132, 2012.

[184] C. Galland. *Quantum Optics with Single-Wall Carbon Nanotubes*. PhD thesis, ETH Zurich, 1983.

[185] S. M. Tabakman, K. Welsher, G. Hong, and H. Dai. Optical properties of single-walled carbon nanotubes separated in a density gradient: Length, bundling, and aromatic stacking effects. *Journal of Physical Chemistry C*, 114(46):19569–19575, 2010.

[186] M. Steiner, M. Freitag, V. Perebeinos, A. Naumov, J. P. Small, A. A. Bol, and P. Avouris. Gate-variable light absorption and emission in a semiconducting carbon nanotube. *Nano letters*, 9(10):3477–81, oct 2009.

[187] S. Yasukochi, T. Murai, S. Moritsubo, T. Shimada, S. Chiashi, S. Maruyama, and Y. K. Kato. Gate-induced blueshift and quenching of photoluminescence in suspended single-walled carbon nanotubes. *Physical Review B*, 84(12):121409, sep 2011.

[188] H. Htoon, M. J. O'Connell, S. K. Doom, and V. I. Klimov. Single carbon nanotubes probed by photoluminescence excitation spectroscopy: The role of phonon-assisted transitions. *Physical Review Letters*, 94(12):1–4, apr 2005.

[189] Z. Luo, F. Papadimitrakopoulos, and S. K. Doorn. Intermediate-frequency Raman modes for the lower optical transitions of semiconducting single-walled carbon nanotubes. *Physical Review B*, 75(20):205438, 2007.

[190] Mukul Kumar and Yoshinori Ando. Chemical Vapor Deposition of Carbon Nanotubes: A Review on Growth Mechanism and Mass Production. *Journal of Nanoscience and Nanotechnology*, 10(6):3739–3758, 2010.

[191] C. Z. Loebick, R. Podila, J. Reppert, J. Chudow, F. Ren, G. L. Haller, A. M. Rao, and L. D. Pfefferle. Selective Synthesis of Subnanometer Diameter Semiconducting Single-Walled Carbon Nanotubes. *Journal of the American Chemical Society*, 132(14):11125–11131, 2010.

[192] H. Okamoto, R. Schilling, H. Schütz, V. Sudhir, D. J. Wilson, H. Yamaguchi, and T. J. Kippenberg. A strongly-coupled Λ-type micromechanical system. pages 1–4, 2016.

[193] A. Castellanos-Gomez, M. Buscema, R. Molenaar, V. Singh, L. Janssen, H. S. J. van der Zant, and Gary A. Steele. Deterministic transfer of two-dimensional materials by all-dry viscoelastic stamping. *2D Materials*, 1(1):11002, 2014.

[194] H. G. Schuster. Reviews of Nonlinear Dynamics and Complexity. *Reviews of Nonlinear Dynamics and Complexity*, pages 1–215, 2009.

[195] T. Briant. *Caracterisation du couplage optomecanique entre la lumiere et un mirror: bruit thermique et effets quantiques.* PhD thesis, Universite Pierre et Marie Curie, 2003.

[196] C. R. Dean, A. F. Young, I. Meric, C. Lee, L. Wang, S. Sorgenfrei, K. Watanabe, T. Taniguchi, P. Kim, K. L. Shepard, and J. Hone. Boron nitride substrates for high-quality graphene electronics. *Nature nanotechnology*, 5(10):722–726, 2010.